

# Automated deep learning segmentation of high-resolution 7 T ex vivo MRI for quantitative analysis of structure-pathology correlations in neurodegenerative diseases

Pulkit Khandelwal<sup>a,b,\*\*</sup>, Michael Tran Duong<sup>a</sup>, Shokufeh Sadaghiani<sup>c</sup>, Sydney Lim<sup>b,d</sup>, Amanda Denning<sup>b,d</sup>, Eunice Chung<sup>b,d</sup>, Sadhana Ravikumar<sup>b,d</sup>, Sanaz Arezoumandan<sup>c</sup>, Claire Peterson<sup>c</sup>, Madigan Bedard<sup>b,d</sup>, Noah Capp<sup>c</sup>, Ranjit Ittyerah<sup>b,d</sup>, Elyse Migdal<sup>c</sup>, Grace Choi<sup>c</sup>, Emily Kopp<sup>c</sup>, Bridget Loja<sup>c</sup>, Eusha Hasan<sup>c</sup>, Jiacheng Li<sup>c</sup>, Karthik Prabhakaran<sup>d</sup>, Gabor Mizsei<sup>d</sup>, Marianna Gabrielyan<sup>c</sup>, Theresa Schuck<sup>e</sup>, Winifred Trotman<sup>c</sup>, John Robinson<sup>e</sup>, Daniel Ohm<sup>c</sup>, Edward B. Lee<sup>e</sup>, John Q. Trojanowski<sup>e,\*</sup>, Corey McMillan<sup>c</sup>, Murray Grossman<sup>c</sup>, David J. Irwin<sup>c</sup>, John Detre<sup>c</sup>, M. Dylan Tisdall<sup>d</sup>, Sandhitsu R. Das<sup>b,c</sup>, Laura E.M. Wisse<sup>f</sup>, David A. Wolk<sup>c</sup>, Paul A. Yushkevich<sup>b,d</sup>

<sup>a</sup>Department of Bioengineering, University of Pennsylvania, Philadelphia, USA

<sup>b</sup>Penn Image Computing and Science Laboratory, University of Pennsylvania, Philadelphia, USA

<sup>c</sup>Department of Neurology, University of Pennsylvania, Philadelphia, USA

<sup>d</sup>Department of Radiology, University of Pennsylvania, Philadelphia, USA

<sup>e</sup>Department of Pathology and Laboratory Medicine, University of Pennsylvania, Philadelphia, Pennsylvania, USA

<sup>f</sup>Department of Diagnostic Radiology, Lund University, Lund, Sweden

---

## Abstract

**Ex vivo** MRI of the brain provides remarkable advantages over in vivo MRI for visualizing and characterizing detailed neuroanatomy, and helps to link microscale histology studies with morphometric measurements. However, automated segmentation methods for brain mapping in ex vivo MRI are not well developed, primarily due to limited availability of labeled datasets, and heterogeneity in scanner hardware and acquisition protocols. In this work, we present a high resolution of 37 ex vivo post-mortem human brain tissue specimens scanned

---

\* Author deceased.

\*\* Corresponding author: Pulkit Khandelwal  
Richards Medical Research Laboratories  
6th Floor 6025, 3700 Hamilton Walk, Philadelphia, PA 19104  
Email address: pulks@seas.upenn.edu

on a 7T whole-body MRI scanner. We developed a deep learning pipeline to segment the cortical mantle by benchmarking the performance of nine deep neural architectures. We then segment the four subcortical structures: caudate, putamen, globus pallidus, and thalamus; white matter hyperintensities, and the normal appearing white matter. We show excellent generalizing capabilities across whole brain hemispheres in different specimens, and also on unseen images acquired at different magnetic field strengths and different imaging sequence. We then compute volumetric and localized cortical thickness measurements across key regions, and link them with semi-quantitative neuropathological ratings. Our code, containerized executables, and the processed datasets are publicly available [here](#).

*Keywords:* 7 T ex vivo MRI, Alzheimer’s Disease, dementia, deep learning, image segmentation

---

## 1. Introduction

Neurodegenerative diseases are increasingly understood to be heterogeneous, with multiple distinct neuropathological processes jointly contributing to neurodegeneration in most patients, called *mixed pathology* Schneider et al. (2007). For example, many patients diagnosed at autopsy with Alzheimer’s disease (AD) also have brain lesions associated with vascular disease, TDP-43 proteinopathy, and  $\alpha$ -synuclein pathology Robinson et al. (2018); Matej et al. (2019). Currently, some of these pathological processes (particularly TDP-43 and  $\alpha$ -synuclein pathologies) cannot be reliably detected with in vivo biomarkers, which makes it difficult for clinicians to determine to what extent cognitive decline in individual patients is driven by AD vs. other factors. The recent modest successes of AD treatments in clinical trials van Dyck et al. (2022) make it ever more important to derive in vivo biomarkers that can detect and quantify mixed pathology, so that treatments can be prioritised for those most likely to benefit from them.

Importantly, the understanding and utility of in vivo biomarkers are aug-

mented by the coupling of imaging and postmortem pathology. Following autopsy, histological examination of the donor’s brain tissue provides a semi-quantitative assessment of the presence and severity of various pathological drivers of neurodegeneration. Associations between these pathology measures and regional measures of neurodegeneration, such as cortical thickness, can identify patterns of neurodegeneration probabilistically linked to specific pathological drivers de Flores et al. (2020); Frigerio et al. (2021); Wisse et al. (2021, 2020). Such association studies can use either antemortem (in vivo) imaging (i.e., MRI scans obtained some time before death) or postmortem (ex vivo) imaging Wisse et al. (2017). Both approaches have their limitations. Antemortem MRI datasets are heterogeneous, and the time between antemortem imaging and death is long, the postmortem pathology may not accurately reflect the state of pathology at the time of imaging. Postmortem MRI generally requires dedicated imaging facilities and image analysis algorithms, and whatever neurodegeneration/pathology association patterns are discovered have to be “translated” into the in vivo imaging domain for use as in vivo biomarkers. However, postmortem MRI allows imaging at much greater resolution than in vivo, allowing structure/pathology associations to be examined with greater granularity than antemortem in vivo imaging.

Furthermore, ex vivo MRI of the brain could provide an advantage over in vivo MRI for visualizing detailed and intricate neuroanatomy and linking macroscopic morphometric measures such as cortical thickness to underlying cytoarchitecture and pathology Mancini et al. (2020); Beaujoin et al. (2018); Pallegage-Gamarallage et al. (2018); García-Cabezas et al. (2020); Augustinack et al. (2010); Vega et al. (2021); Alkemade et al. (2022); Iglesias et al. (2015); Adler et al. (2014). Recent inquiries comparing ex vivo imaging with histopathology have demonstrated relationships between atrophy measures and neurodegenerative pathology Wisse et al. (2021); Ravikumar et al. (2021); Yushkevich et al. (2021); Makkinejad et al. (2019). Such associations corroborate patterns of neurodegeneration by specifically linking them with the underlying contributing pathology such as TDP-43, p-tau and  $\alpha$ -synuclein in Alzheimer’s Disease

(AD). Ex vivo imaging also helps in characterizing underlying anatomy at the scale of subcortical layers Augustinack et al. (2013); Kenkhuis et al. (2019), such as hippocampal subfields in the medial temporal lobe (MTL) Yushkevich et al. (2021); Ravikumar et al. (2020). Several studies have also explored pathology/MRI associations in other neurodegenerative diseases, such as Frontotemporal lobar degeneration (FTLD), Amyotrophic lateral sclerosis (ALS) Gordon et al. (2016); Irwin et al. (2015); Mackenzie et al. (2011). Previous work has identified correlations between high resolution ex vivo MRI and histopathology, to map myelin and iron deposits in cortical laminae Bulk et al. (2020), due to oligodendrocytes and pathologic iron inclusions in astrocytes and microglia Tisdall et al. (2021), which are a major source of iron because of myelination demands. Therefore, ex vivo MRI would be helpful for validating and refining pathophysiological correlates derived from in vivo studies.

Compared to in vivo MRI, ex vivo MRI is not affected by head or respiratory motion artifacts and has much less stringent time. Compared to histology, it does not suffer from distortion or tearing of brain tissue, thereby giving flexibility in acquiring high resolution images. Indeed, ex vivo MRI is often used to provide a 3D reference space onto which 2D histological images are mapped. Combined analysis of ex vivo MRI and histology makes it possible to link morphological changes in the brain to underlying pathology as well as to generate anatomically correct parcellations of the brain based on cytoarchitecture Schiffer et al. (2021c); Amunts et al. (2020), and pathoarchitecture Augustinack et al. (2013). ex vivo MRI could also act as a reference space to generate quantitative 3D maps of neurodegenerative proteinopathies from serial histology imaging Ushizima et al. (2022); Yushkevich et al. (2021).

Given the rising use of high resolution ex vivo MRI in neurodegenerative disease research, automated techniques are imperative to effectively analyze such growing datasets. Particularly, in the case of structure-pathology association studies, scaling them beyond a few dozen datasets requires reliable morphometry measurements from ex vivo MRI via accurate 3D segmentation and reconstruction of the structures of interest. There has been substantial work in brain MRI

parcellation such as *FreeSurfer* Fischl (2012) and recent efforts based on deep learning Henschel et al. (2020); Chen et al. (2018). However, these approaches focus on in vivo MRI, and there is limited work on developing automated segmentation methods for ex vivo MRI segmentation. ex vivo segmentation methods have been region specific. Recent developments include automated deep learning methods for high resolution cytoarchitectonic mapping of the occipital lobe in 2D histological sections [Schiffer et al. (2021c); Spitzer et al. (2018); Kiwitz et al. (2020); Schiffer et al. (2021a,b); Eckermann et al. (2021)]. The work by Iglesias et al. (2015, 2018) has developed an atlas to segment the MTL and the thalamus using manual segmentations in ex vivo images. Yet, an ex vivo segmentation method applicable to a variety of brain regions has yet to be described. This is attributable to several factors. Some groups have developed robust whole brain ex vivo image analysis tools Jonkman et al. (2019); Mancini et al. (2020); Edlow et al. (2019), though overall there is limited availability of ex vivo specimens, scans, segmentation algorithms and labeled reference standard segmentations. Compared to in vivo structural MRI, ex vivo MRI currently exhibits substantial heterogeneity in scanning protocols, larger image dimensions, greater textual complexity, and more profound artifacts. These issues can be addressed with new datasets and automated segmentation tools open to the public.

In this study, we expand upon our pilot study Khandelwal et al. (2021, 2022a,b) and develop a methodological framework to segment cortical gray matter; subcortical structures (caudate, putamen, globus pallidus, thalamus), white matter (WM) and white matter hyperintensities (WMH) in high resolution ( $0.3 \times 0.3 \times 0.3 \text{ mm}^3$ ) 7 T ex vivo MRI scans of whole brain hemispheres. We train and evaluate our approach using 37 brain hemisphere scans from the Center for Neurodegenerative Disease Research of the University of Pennsylvania. We measure cortical thickness at several key locations in the cortex based on our automatic segmentation of the cortex, and correlate these measures with thickness measurements obtained using a user-guided semi-automated protocol. High consistency between these two sets of measures supports the use of deep

learning-based automated thickness measures for ex vivo brain segmentation and morphometry. We then report regional patterns of association between morphometric measurements (cortical thickness, subcortical structure, WMH and WM volumes) and neuropathology ratings (regional measures of p-tau, neuronal loss, amyloid- $\beta$ ; as well as global Braak staging and CERAD of amyloid- $\beta$  and p-tau pathology), obtained from histology data. Additionally, we show that networks trained on T2-weighted spin echo images acquired at 7 T generalize to ex vivo images obtained with T2\*-weighted (T2\*w) gradient echo images acquired at 7 T, and ex vivo images acquired at 3 T.

## 2. Materials

### 2.1. Donor Cohort

We analyze a dataset of 37 ex vivo whole-hemisphere MRI scans selected from Penn Integrated Neurodegenerative Disease Database (INDD) Toledo et al. (2014). Patients were evaluated at the Penn Frontotemporal Degeneration Center (FTDC) or Alzheimer’s Disease Research Center (ADRC) and followed to autopsy at the Penn Center for Neurodegenerative Disease Research (CNDR) as part of ongoing and previous clinical research programs Tisdall et al. (2021); Irwin (2016); Arezoumandan et al. (2022). The cohort included 12 female (sex assigned at birth) donors (Age:  $75.42 \pm 8.62$  years, Age range: 50-99) and 25 male donors (Age:  $76.68 \pm 11.67$  years, Age range: 63-89) with Alzheimer’s Disease or Related Dementias (ADRD), such as Lewy Body Disease (LBD), Frontotemporal Lobar Degeneration with TAR DNA-binding protein 43 (FTLD-TDP43), Progressive Supranuclear Palsy (PSP), or cognitively normal adults. Human brain specimens were obtained in accordance with local laws and regulations, and includes informed consent from next of kin at time of death. The patients were evaluated at FTDC and ADRC as per standard diagnostic criteria Toledo et al. (2014), and imaged by the teams at ADRC and Penn Image Computing and Science Laboratory (PICSL) and FTDC. Autopsy was performed at the Penn Center for Neurodegenerative Disease Research (CNDR). Figure 1 shows

an example of a brain specimen with Parkinson’s and LBD ready for autopsy, with the slabbed slices shown in Supplementary Figure 1. Separately, the post-mortem tissue photograph of a specimen with progressive non-fluent aphasia (PFNA) and Globular glial tauopathy (GGT) disease is shown in Supplementary Figure 2. Table 1 details the primary neuropathological diagnostic groups in the cohort with additional details tabulated in Supplementary Table 1.

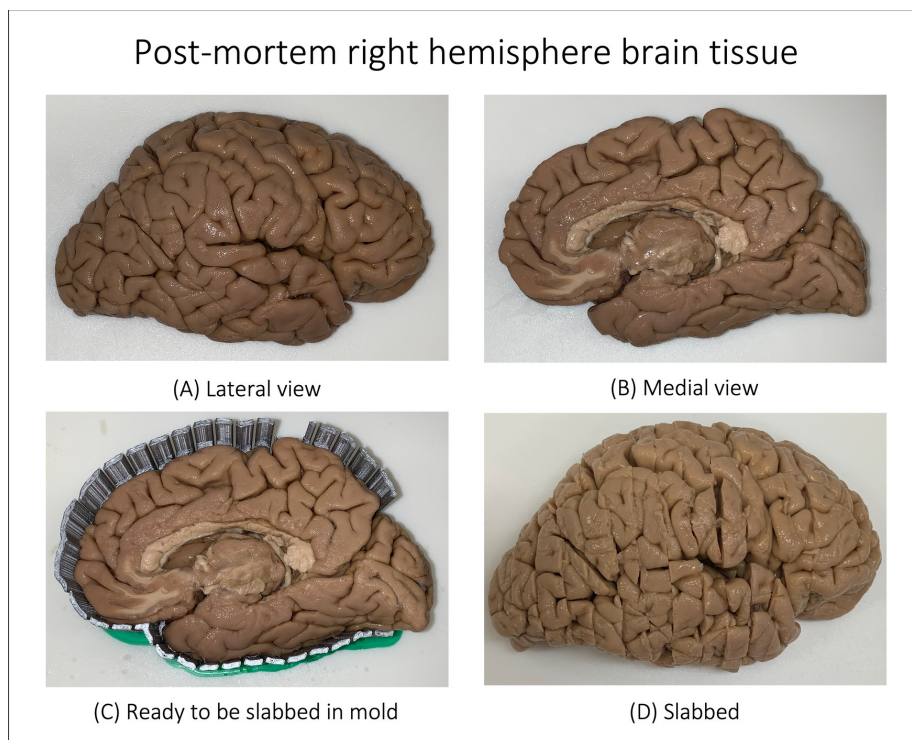


Figure 1: Post-mortem tissue blockface photograph of a donor with diagnosis of Parkinson’s disease (not demented) and Lewy body disease (white female, deceased at the age of 79). Shown are the lateral and medial views of the right hemisphere. The tissue is then placed in a mold and is subsequently slabbed as shown in the bottom right panel. See Supplementary Figure 1 for the slabbed slices of the given brain tissue.

## 2.2. MRI Acquisition

During the autopsy of a specimen, one hemisphere was immersed in 10% neutral buffered formalin for at least 4 weeks prior to imaging. After the fixation time, samples were placed in Fomblin (California Vacuum Technology;

Table 1: Demographics of the Alzheimer’s Disease and Related Dementia (ADRD) patient cohort in the current study. Abbreviations: AD: Alzheimer’s Disease, ALS: Amyotrophic lateral sclerosis, CVD: Cerebrovascular Disease, LATE: Limbic-predominant Age-related TDP-43 Encephalopathy, LBD: Lewy Body Disease, CTE:, FTLT-DTP: Frontotemporal lobar degeneration with TDP inclusions, GGT: Globular glial tauopathy, CVD: Cerebrovascular Disease, CBD: Corticobasal degeneration, PART: Primary age-related tauopathy, PSP: Progressive supranuclear palsy, tau-Misc: tauopathy unclassifiable.

Brain donor cohort							
N	37 (Female: 12 and Male: 25)						
Age (years)	74.55 ± 10.94 (range 50-99)						
Race	White: 33 Black: 3 Unknown: 1						
Hemisphere imaged	Right:14 Left: 23						
Post-mortem interval (hours)	16.35 ± 10.01						
Neuropathological diagnosis							
	Primary			Secondary/ tertiary			
Alzheimer’s disease	18			9			
Lewy body disease	3			5			
PART	1						
Cerebrovascular disease	1			2			
LATE				6			
FTLD-TDP	8						
Tau-Misc (unclassifiable and FTLD-17)	2						
Corticobasal degeneration	1			1			
Tau-4R	2						
Hippocampal Sclerosis				2			
Progressive supranuclear palsy	1						
Amyotrophic lateral sclerosis (ALS)				1			
Global neuropathological staging							
Ratings	0	1	2	3			
Amyloid-β Thal staging (A score)	3	8	9	17			
Braak three stage scheme (B score)	4	10	9	13			
CERAD (C score)	12	6	6	14			
Six-stage Braak scheme	0	1	2	3	4	5	6
	4	2	8	5	4	3	10

Fremont, CA), enclosed in custom-built plastic bag holders. Samples were left to rest for at least 2 days to allow the air bubbles to escape from the tissue. The samples were scanned using either a custom-built small solenoid coil or a custom-modified quadrature birdcage (Varian, Palo Alto, CA, USA) coil Tisdall et al. (2021); Edlow et al. (2019). The samples were then placed into a whole-body 7 T scanner (MAGNETOM Terra, Siemens Healthineers, Erlangen, Germany). T2-weighted images were acquired using a 3D-encoded T2 SPACE sequence with  $0.3 \times 0.3 \times 0.3 \text{ mm}^3$  isotropic resolution, 3 s repetition time (TR), echo time (TE) 383 ms, turbo factor 188, echo train duration 951 ms, bandwidth 348 Hz/px in approximately 2-3 hours per measurement. Image reconstruction was done using the vendor’s on-scanner reconstruction software which also corrected the global frequency drift, combined the signal averages in k-space, and produced magnitude images for each echo. A total of 4 repeated measurements were acquired for each sample and subsequently averaged to generate the final image. Sample MRI slices are shown in Figure 2 for a range of specimens with different diseases. The image acquisition suffers from geometric distortions due to the non-linearity of the magnetic gradient field that increases towards the ends (both anterior and posterior) of the sample and B1-transmit inhomogeneity, which results in decreased image quality as shown in Figure 2.

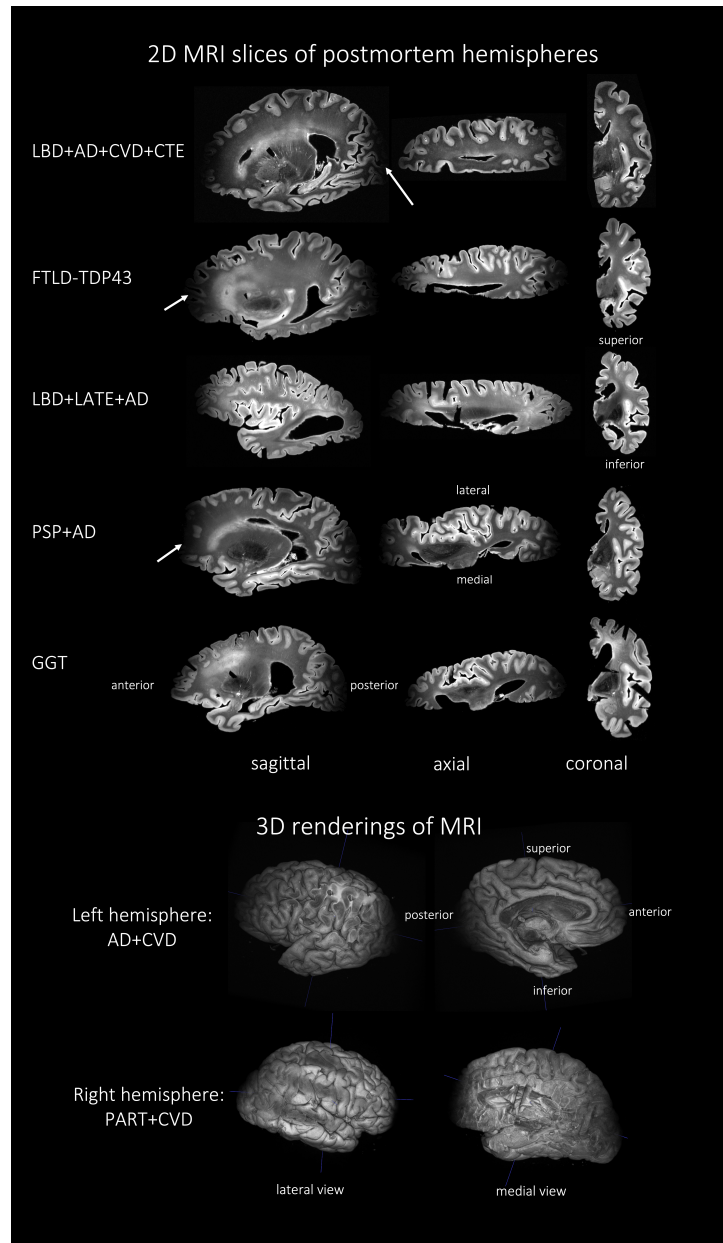


Figure 2: Two-dimensional MRI slices of the T2w sequence representative of ADRD spectrum with mixed pathology and diagnoses of five subjects. The heterogeneity amongst the subjects can be appreciated through the three different viewing planes. Notice that the MRI signal drops off at the anterior and posterior ends of the hemisphere, a drawback of the current acquisition protocol. Also shown are the three-dimensional MRI renderings of the left and right brain hemispheres of two different subjects. Abbreviations: AD: Alzheimer's Disease, ALS: Amyotrophic lateral sclerosis, CVD: Cerebrovascular Disease, LATE: Limbic-predominant Age-related TDP-43 Encephalopathy, LBD: Lewy Body Disease, CTE: Frontotemporal lobar degeneration with TDP inclusions, FTLD-TDP: Globular glial tauopathy, GGT: Cerebrovascular Disease, CBD: Corticobasal degeneration, PART: Primary age-related tauopathy, PSP: Progressive supranuclear palsy, tau-Misc: tauopathy unclassifiable.

### 2.3. Neuropathological ratings

The non-imaged hemisphere, i.e., the contralateral tissue of each specimen systematically underwent histological processing for neuropathological examination at the CNDR Toledo et al. (2014). Roughly  $1.5 \times 1.5 \times 0.5 \text{ cm}^3$  tissue blocks were extracted from the contralateral hemisphere. Paraffin-embedded blocks were then sectioned into  $6 \mu\text{m}$  for immunohistochemistry using phosphorylated tau (AT8; Fisher, Waltham, MA; Catalogue No. ENMN1020) to detect phosphorylated p-tau deposits and p409/410 (mAb, 1:500, a gift from Dr. Manuela Neumann and Dr. E. Kremmer) to detect phosphorylated TDP-43 deposits. Immunohistochemistry evaluation was performed on the hemisphere contralateral to the hemisphere that was scanned using previously validated antibodies and established methods22: NAB228 (monoclonal antibody [mAb], 1:8000, generated in the Center for Neurodegenerative Disease Research [CNDR]), phosphorylated tau PHF-1 (mAb, 1:1000, a gift from Dr. Peter Davies), TAR5P-1D3 (mAb, 1:500, a gift from Dr. Manuela Neumann and Dr. E. Kremmer), and Syn303 (mAb, 1:16,000, generated in the CNDR) to detect amyloid beta ( $A\beta$ ) deposits, phosphorylated tau (p-tau) deposits, phosphorylated TDP-43 deposits, and the presence of pathological conformation of  $\alpha$ -synuclein, respectively. In 16 cortical regions, semi-quantitative ratings of p-tau, TDP-43, beta-amyloid, and  $\alpha$ -synuclein pathology, as well as neuronal loss, were visually assigned by an expert neuropathologist (E.L. and J.Q.T.) on a scale of 0–3 i.e. “0: None”, “0.5: Rare”, “1: Mild”, “2: Moderate” or “3: Severe” Toledo et al. (2014). These ratings are illustrated in Figure 3. Global ratings of neurodegenerative disease progression were also derived, including A, B, C scores Hyman et al. (2012). Supplementary Table 2 details the locations from where the neuropathology ratings were obtained from, either the exact (main regions) or the closest (exploratory regions), to the cortical brain regions.

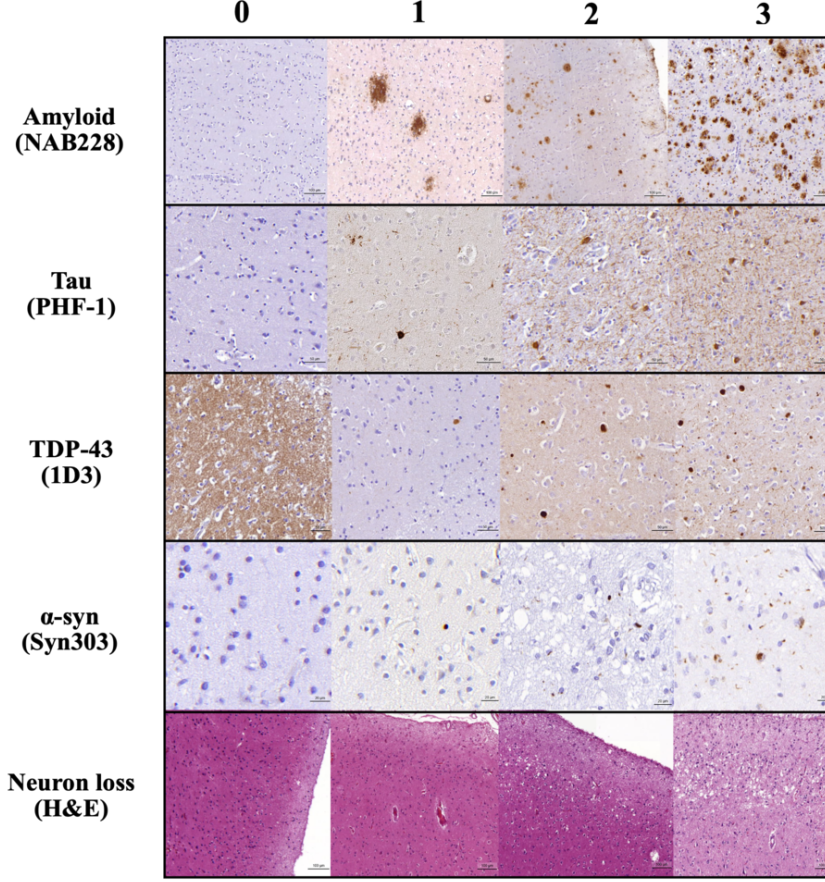


Figure 3: Pathological assessment for each regional pathology derived from histology as per the protocol discussed in Section 2.3. The columns are severity ratings (left to right): 0-3. The shown pathologies are: amyloid- $\beta$  plaques (NAB228 antibody), p-tau pathology (PHF-1 antibody), TDP-43 inclusions (pS409/410 antibody), Lewy bodies (Syn303 antibody) and neuron loss (Hematoxylin and Eosin staining) in different cortical and medial temporal lobe regions included in the current work. Scale bars are shown for reference.

#### 2.4. Localized thickness measurement pipeline at key cortical locations

Our center has adopted a expert-supervised semi-automatic protocol to obtain localized quantitative measures of cortical thickness in all 7 T ex vivo MRI scans, as described in the work by Sadaghiani et al. (2022) Section 2.3 and

Supplemental material S1, Wisse et al. (2021) Section: MTL thickness measurements and Supplemental material: Thickness measurement. In the current study, we use these measures as the reference standard for evaluating automated cortical segmentation. In each hemisphere, 16 cortical landmarks are identified and labeled on the MRI scan as shown in Figure 4 A. To measure cortical thickness at these locations, a semi-automatic level set segmentation of the surrounding cortical ribbon is performed and the maximal sphere inscribed into the cortical segmentation and containing the landmark is found; the diameter of this sphere gives thickness at that landmark (Figure 4 B).

## Cortical landmark locations

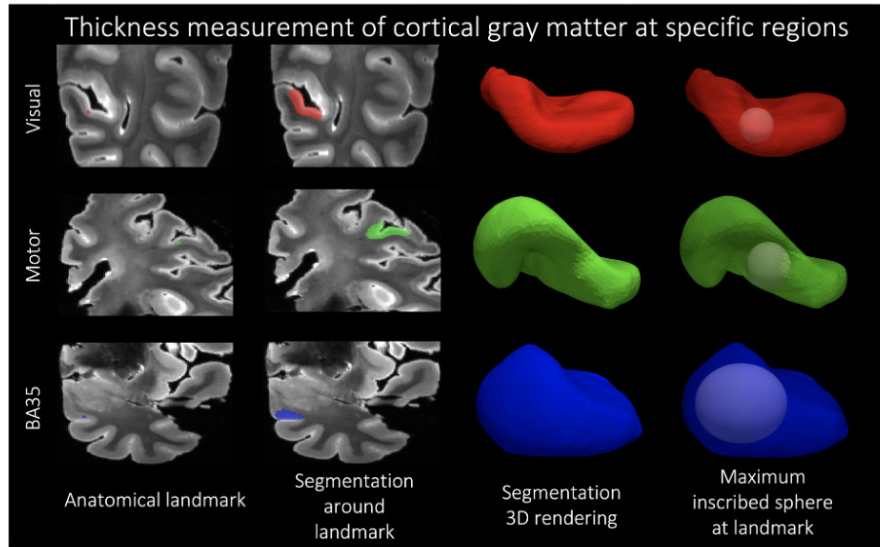
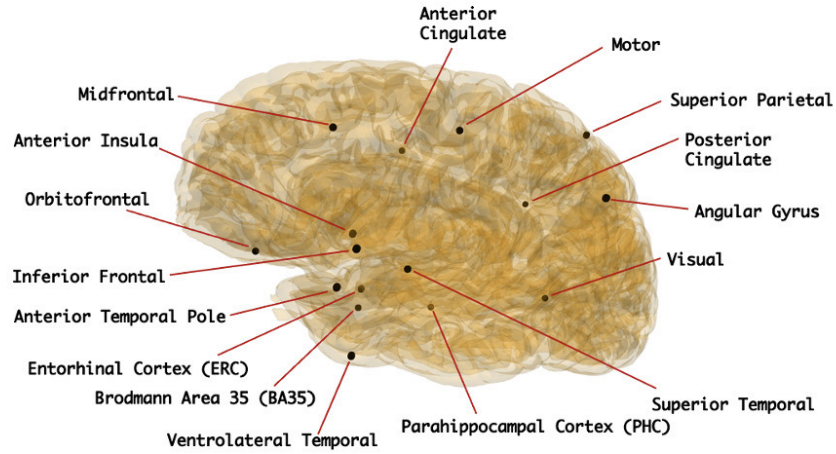


Figure 4: Cortical thickness is measured at the 16 landmarks. A dot (shown here: motor, visual, BA35) is first placed to define an anatomical landmark, around which a semi-automatic level set segmentation of the surrounding cortical ribbon is provided. A maximally inscribed sphere is then computed using Voronoi skeletonization Ogniewicz and Ilg (1992), and the diameter of the sphere gives thickness at that landmark.

### 3. Methods

In Section 3.1, we describe the manual segmentation protocols developed for cortical gray matter, four subcortical structures, white matter hyperintensities, and normal-appearing white matter. Then, in sections 3.2 and 3.3, we describe the deep learning-based pipeline and performance evaluation criteria developed for the automated segmentation of these structures. Finally, in section 3.4, we describe the statistical models used to link neuropathological ratings of p-tau, amyloid- $\beta$  neuronal loss, CERAD scores, Braak Staging with morphometry based on volume and regional thickness measurements obtained from the automated segmentations.

#### 3.1. Manual segmentation protocols

We developed protocols to manually segment structures in ex vivo MRI: cortical gray matter, subcortical structures (caudate, putamen, globus pallidus, thalamus), WM, and WMH. We used these manual segmentations along with the corresponding MR images to train the neural networks. All manual segmentations were done by raters in ITK-SNAP Yushkevich et al. (2019). Supplementary Table 1 shows which subjects were manually segmented to obtain the training data and the reference standard for the different labels, and the subsequent cross-validation studies as described in Sections 3.2 and 3.3.

##### 3.1.1. Cortical Gray Matter

We sampled five 3D image patches of size 64 x 64 x 64 voxel<sup>3</sup>, as shown in Figure 5 around the orbitofrontal cortex (OFC), anterior temporal cortex (ATC), inferior prefrontal cortex (IPFC), primary motor cortex (PMC), and primary somatosensory cortex (PSC) from 6 brain hemispheres, resulting in a total of 30 patches. These regions were selected as representative regions with variable levels of pathology in ADRD cases and control regions (PMC, PSC) Tisdall et al. (2021). For example, OFC, ATC and IPFC have high pathology in PSP, whereas, the PSC, which is generally less-affected in most neurodegenerative diseases, was sampled as a negative control. In each patch, gray matter

was segmented manually in ITK-SNAP. Five manual raters, divided into groups of two (E.K. and G.C.) and three (E.H, B.L.P. and E.M.), labeled gray matter as the foreground, and rest of the image as the background using a combination of manual tracing and the semi-automated segmentation tool. The manual segmentation of cortical gray matter was supervised by author P.K. Figure 5 shows sample patch images and the corresponding reference standard labels with 3D renderings. We followed some guiding principles for manual segmentation: (1) we note that the white layer enveloping the cortex is not an imaging artifact, but is the outermost layer of the cortex, and thus is labeled as the gray matter, (2) adjoining gyri in deep sulci region are correctly labeled as gray matter and demarcates the deep sulci as the background. (3) in several regions, gray matter have similar intensities with the nearby WMH which were resolved by visual inspection of texture in the surrounding region, (4) the 64x64x64 patches provided little context when segmenting the GM, therefore, the corresponding whole hemisphere image was displayed on a separate ITK-SNAP window for the user to examine the structures surrounding the given image patch. Inter-rater reliability scores were computed for these manual segmentations in terms of Dice Coefficient (DSC): Raters 1&2:  $95.26 \pm 1.37$  %, Raters 1&3:  $94.64 \pm 1.64$  %, Raters 2&3:  $94.54 \pm 1.20$  %, Raters 4&5:  $92.04 \pm 4.26$  %.

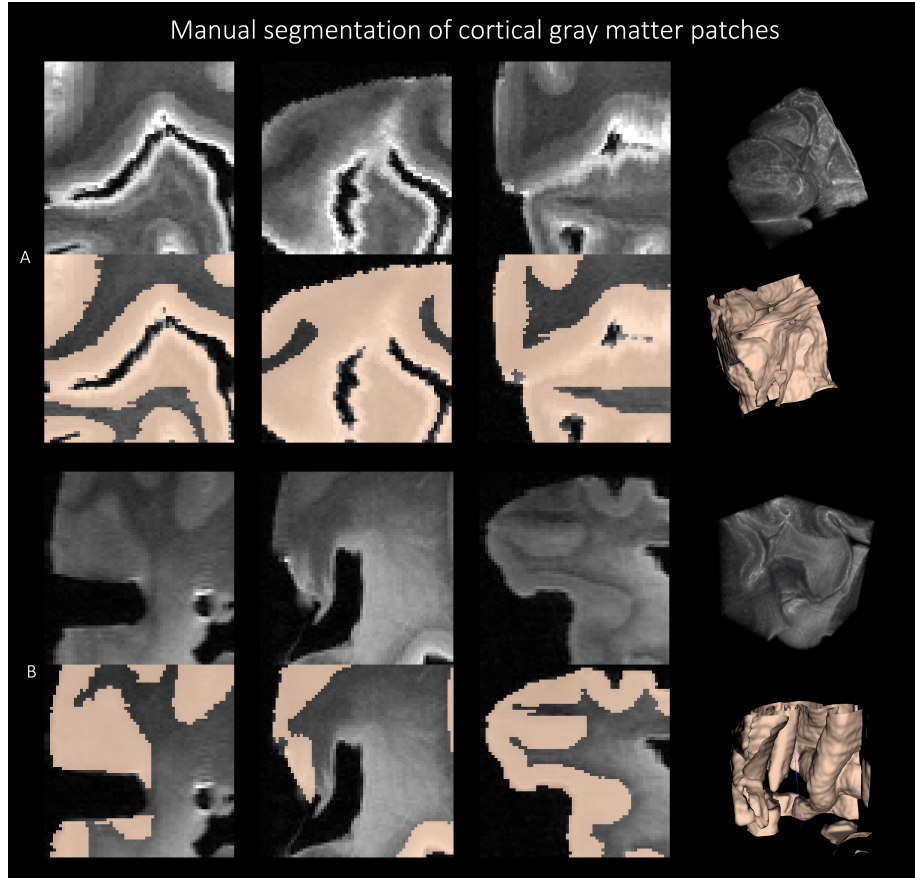


Figure 5: Manual segmentation of the cortical gray matter patches of size  $64 \times 64 \times 64$  using the protocol explained in 3.1.1 for two subjects with FTLD-TDP (top) and GGT (bottom) in three viewing planes with the corresponding 3D renderings.

### 3.1.2. Subcortical structures

Four subcortical gray matter structures (caudate, putamen, globus pallidus, thalamus) were manually segmented on 7 specimens, selected to span varying pathological diagnoses (including Alzheimer’s spectrum, p-tauopathies, TDP-43 encephalopathies, LBD, cerebrovascular disease and mixed disease), the range of postmortem age and levels of cerebral atrophy, tissue quality and tearing, mineral deposition and calcification, blood vessel size, vascular pathology on imaging and autopsy. Figure 6 shows an example manual segmentation of the four subcortical structures. First, structures were segmented across the ax-

ial plane based on several anatomical considerations. (1) The borders of the caudate (head, body and tail) were defined by the frontal horns of the lateral ventricles (cerebrospinal fluid, anterior border) and the internal capsule (WM, boundaries of the body). Periventricular WM disease adjacent to the head of the caudate was excluded from the caudate segmentation. (2) The borders of the putamen were determined by the globus pallidus (medial) and the claustrum (lateral). (3) The globus pallidus was annotated to include the pallidum interna and externa, bounded by WM surrounding the thalamus and subthalamic nucleus. Mineral deposition (such as calcium) was noted by areas of heterogeneous T2 hypointensities and predominantly localized to the lentiform nucleus; where needed, the contours of some segmentations were adjusted to include these regions of heterogeneous signal within the lentiform structures. (4) The thalamus was segmented as the medial gray matter bounded by the subthalamic nucleus, midbrain, mamillary bodies, corpus callosum, lateral ventricles and caudate. After segmentation in the axial plane, volumes were edited in the coronal and sagittal planes to ensure smoothness of the segmentation across all three planes. Boundaries between structures (such as striations between caudate and putamen) were agreed upon among authors. Manual segmentation of the four subcortical structures was performed by author, E.C. and supervised by and edited by M.T.D. Subcortical segmentations were discussed in consensus meetings with P.K., P.A.Y, S.R.D and D.A.W.

### *3.1.3. White Matter Hyperintensities*

Nine specimens were chosen to segment WMHs across a gamut of vascular pathology with differing levels of WMH appearance, including focal small-vessel ischemia to intermediate periventricular and juxtacortical patterns to large, diffuse cerebrovascular disease. General principles for segmentation were applied as follows. (1) segmented lesions should be generally larger than  $1 \text{ cm}^3$ , (2) segmentations should appear for at least 4-6 slices to be a  $1 \text{ cm}^3$  region, (3) segmented WMH should include both periventricular (anterior frontal and posterior temporal/occipital horns of the lateral ventricles) and juxtacortical lesions. This

distinguished WMH from insular cortex, claustrum, basal ganglia and other gray matter structures embedded in WM. (4) WMH segmentations generally exhibited signal intensity above a threshold of  $\geq 450$ -550 intensity, (but this was influenced by field inhomogeneity artifacts, either between images or within the same image, often at the anterior and posterior cortical poles), given the image intensity range was normalized between 0-1000. (5) WMH segmentations included T2 hyperintense perivascular spaces and cortical venules but must also include surrounding T2 hyperintense white matter regions that occupy a region larger than  $1 \text{ cm}^3$ . (6) WMH was segmented primarily in axial plane and then assessed for contiguity and smoothness in sagittal and axial planes as well as 3D renderings. Manual segmentation was performed by the author A.D. and supervised and edited by M.T.D. WMH segmentations were discussed in consensus meetings with P.K., P.A.Y, S.R.D and D.A.W. Figure 6 shows an example manual segmentation of the white matter hyperintensities.

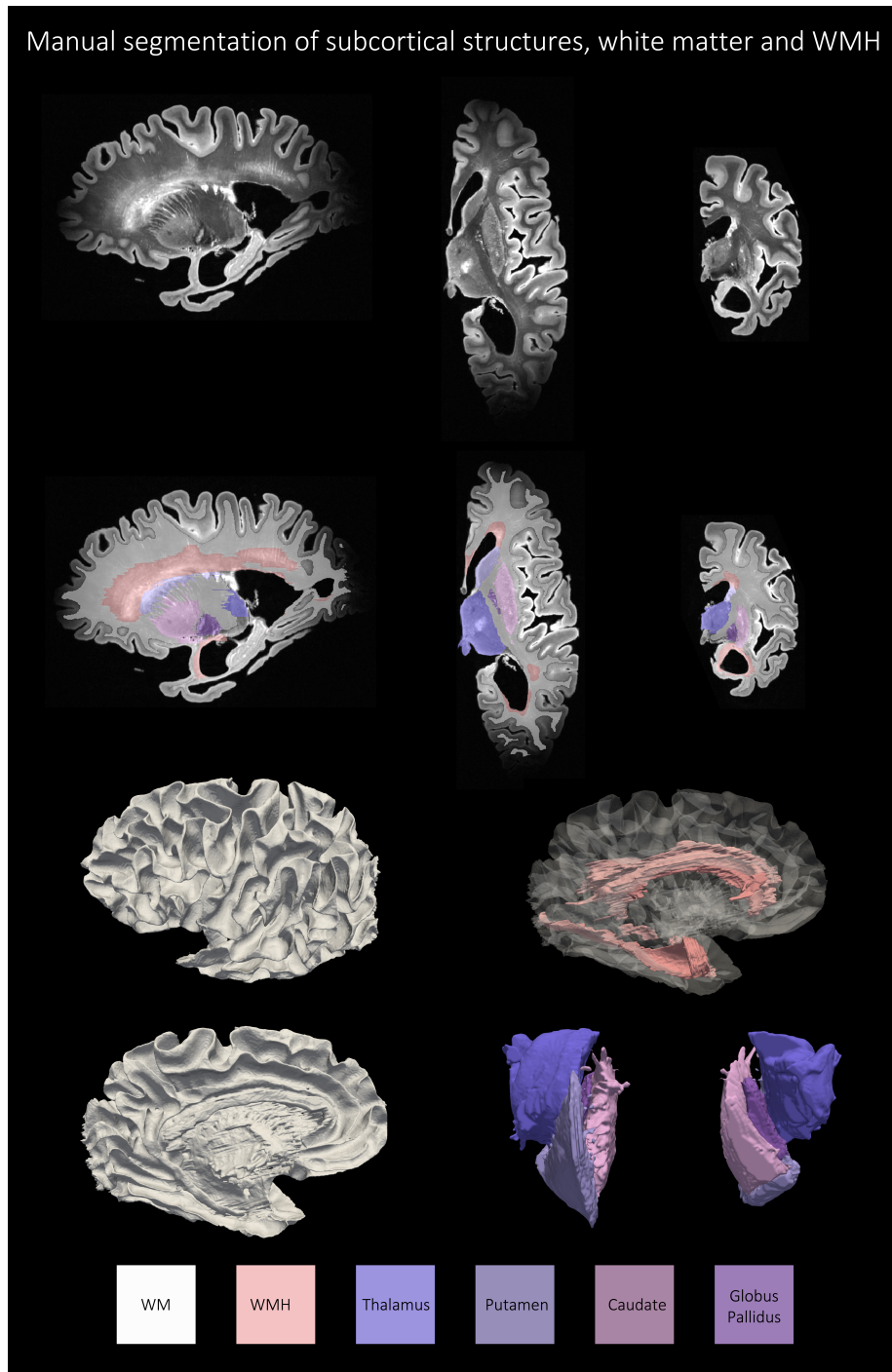


Figure 6: An example of manual segmentation of the thalamus, putamen, caudate, globus pallidus and white matter hyperintensities as per the protocol described in Sections 3.1.2 and 3.1.3 for a subject with Alzheimer's Disease and Lewy body disease (87 years old, white male). 20

#### 3.1.4. *White Matter*

Two specimens with manually labelled subcortical structures, WMH but automated segmentations for cortical mantle were thresholded to obtain the WM label, which was then manually corrected by the author A.D., supervised by P.K., to remove incorrectly labeled spurious voxels to fill-in holes and thereby define a clear GM/WM boundary.

#### 3.2. *Automated deep learning-based segmentation for cortical gray matter*

We first developed an approach for labeling cortical gray matter in ex vivo 7 T MRI scans using the 30 patch-level cortical gray matter segmentations from six subjects (described in Section 3.1.1) for training and cross-validation. Given the exceptional performance of convolutional neural network (CNN) models for in vivo medical image segmentation Schiffer et al. (2021c), our effort focused on benchmarking leading existing CNN models, rather than developing another model for the ex vivo cortical segmentation task. We benchmark the following variants of popular biomedical image segmentation deep learning models: (1) nnU-Net Isensee et al. (2021); four variants of AnatomyNet Zhu et al. (2019) based on squeeze-and-excitation blocks Roy et al. (2018): (2) Channel Squeeze and Spatial Excitation AnatomyNet (SE), (3) Spatial Squeeze and Channel Excitation AnatomyNet (CE), (4) AnatomyNet (Vanilla), (5) Spatial and Channel Squeeze and Excitation AnatomyNet (SE + CE); (6) 3D Unet-like network Khandelwal and Yushkevich (2020); (7) VoxResNet Chen et al. (2018); (8) VNet Milletari et al. (2016) ; and (9) Attention Unet Oktay et al. (2018). Supplementary Section 2 provide architectural details of the nine deep neural networks. We use PyTorch 1.5.1 and Nvidia Quadro RTX 5000 GPUs to train the models using user-annotated images described as described in Sections 3.1.1 - 3.1.3. To train the deep neural networks, the input images were standardized, and then normalized between 0 and 1.

To ensure a fair and systematic evaluation of the nine networks, we trained and evaluated the nine network architectures within the nnU-Net framework under matched conditions (i.e., same split of data into training/validation/testing

subsets; same data augmentation strategy, same hyper-parameter tuning strategy). We first evaluated the accuracy of cortical segmentation by six-fold cross-validation on the patch-level manual segmentations. We report average DSC and average Hausdorff Distance 95th percentile (HD95) across the 30 segmented patches in the six-fold cross-validation experiments.

The nine trained models were then used to segment the whole hemisphere cortical mantle across the 37 specimens. We used these segmentations to compute the thickness around the 16 landmarks described in Section 2.4 in each specimen. We then compared these thickness measurements to corresponding measures obtained using our semi-automated protocol (Section 2.4). For each of the 16 landmarks, we report Spearman’s correlation coefficient between the automated and manual segmentation-based cortical thickness measurements, and the average fixed raters intra-class correlation coefficient (ICC). Based on the combination of cross-validation DSC accuracy, agreement between the automatic and manual segmentation-based cortical thickness measures, and overall visual inspection of the segmentations, a single model was selected for subsequent experiments. As reported in Section 4.1, this best-performing method was the **nnU-Net** model.

### *3.3. Automated deep learning-based segmentation for other structures*

The **nnU-Net** model was used for the automated segmentation of subcortical structures, WMH and normal-appearing WM. For the purpose of five-fold cross-validation studies to report DSC and HD95 scores, we trained separate nnU-Net models based on the manually-labeled training data for the segmentation of subcortical structures in 7 subjects and WMH in 9 subjects respectively with automated entire cortical mantle and manually labelled WM as the other classes.

### *3.4. Linking neuropathology ratings with morphometry*

We computed Spearman’s correlation between thickness measurements obtained from automated segmentations at the 16 anatomical landmarks described

above with semi-quantitative pathology ratings from approximately corresponding anatomical locations in the contralateral hemisphere (regional p-tau score, regional neuronal loss) and global pathology ratings (CERAD stage, Braak stage). We repeat this analysis with thickness measurements obtained from user-annotated manual segmentations, and thereby test the hypothesis that similar trends would be seen between pathology correlations with automated and manual thickness measures, which, in turn, would imply that automated segmentations are viable for morphometry-based studies (Section 4.4). In particular, we follow the experimental design from our recent work Sadaghiani et al. (2022) for a subset of the cohort with AD as the primary diagnosis (N=22) out of 37. However, we do not include the nuisance covariates (age, sex and postmortem interval) because the objective here is to compare between automatic and semi-automatic thickness measurements rather than describe the structure/pathology correlations from a clinical perspective.

We compared the volumes of subcortical structures in a pairwise manner across five diagnostic categories: AD spectrum, LBD, FTLD, tauopathy 4 repeat (4R), tauopathy Miscellaneous (Section 4.4.2). Subcortical volumes were adjusted for intracranial volume (ICV): Antemortem in vivo MRI scans were available for 27 out of 37 ex vivo brain donors. In these 27 donors, ICV was computed via the ASHS pipeline Yushkevich et al. (2015); Xie et al. (2019). For the remaining 10 donors, ICV was imputed (i.e., set equal to the mean ICV of the 27 donors with 3 T in vivo scans.). Finally, we normalized the WMH volumes by the corresponding WM volumes, and then computed one-sided Spearman correlation between the normalized WMH volume with regional cortical thickness and subcortical volumes.

## 4. Results

### 4.1. Cortical Gray Matter Segmentation

#### 4.1.1. Dice coefficient volume overlap and qualitative analysis

Table 2: Six-fold cross validation Dice Coefficient (DSC) and Hausdorff Distance 95th percentile (HD95) scores between reference standard and automated patch-level segmentations.

Deep learning method	DSC (%)	HD95 (mm)
nnU-Net	$93.98 \pm 5.25$	$0.49 \pm 0.45$
AnatomyNet (SE)	$94.84 \pm 3.84$	$0.45 \pm 0.42$
AnatomyNet (CE)	$94.91 \pm 3.27$	$0.45 \pm 0.42$
AnatomyNet (Vanilla)	$94.86 \pm 3.83$	$0.46 \pm 0.44$
AnatomyNet (CE + SE)	$94.66 \pm 3.79$	$0.47 \pm 0.44$
3D Unet	$93.57 \pm 5.22$	$0.58 \pm 0.51$
VoxResNet	$94.84 \pm 4.00$	$0.45 \pm 0.42$
VNet	$90.84 \pm 5.93$	$0.99 \pm 0.56$
Attention Unet	$93.65 \pm 4.91$	$0.62 \pm 0.66$

Table 2 tabulates the *patch*-level cortical gray matter segmentation performance of the nine different networks across six-fold cross validation. AnatomyNet and its variants attain the highest patch-level DSC, closely followed by VoxResNet. The nnU-Net model has slightly lower DSC than the best AnatomyNet model, but the difference is less than 1%. However, since the patches used to train the segmentation networks were only sampled from select regions of the hemispheres, cross-validation accuracy on these patches is not necessarily indicative of the networks’ ability to generalize to other brain regions. Figure 7 illustrates, that consistently across our specimens, AnatomyNet and its variants are able to distinguish gray matter from white matter in high-contrast regions, but fail to segment the anterior and posterior regions where contrast is lower due to limitations of the MRI coil. There is also some systematic under-segmentation (see white arrows) of the cortex even in higher-contrast regions

(see the white circled regions in Figure 7). By contrast, nnU-Net clearly demarcates GM/WM boundary even in low-contrast regions, which is remarkable considering that these regions were not captured by the training patches.

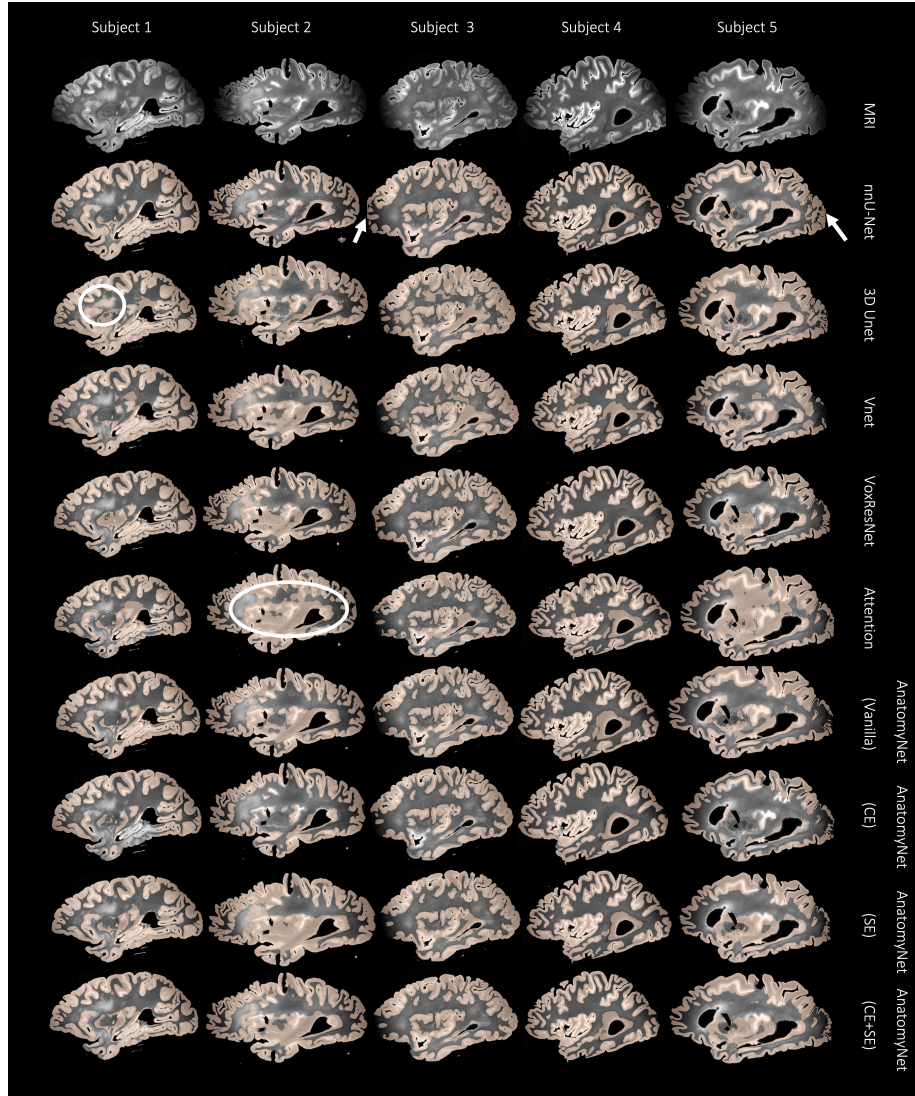


Figure 7: For a subset of 10 subjects, each row shows an example sagittal view of the automated cortical mantle segmentation predicted across the whole brain hemisphere using the different neural network architectures. We notice that all architectures except nnU-Net shows either under- or over-segmentation of the cortical gray matter, which, together with the results reported in Table 2 (ICC results) prompted us to select nnU-Net as the preferred model for cortical gray matter segmentation. For example, notice that how networks such as 3D Unet and Attention Unet incorrectly segments large chunks of WM as cortical GM (white circles). Whereas, nnU-Net performs the best in difficult to segment areas such as the anterior and posterior regions of the brain with poor MRI signal.

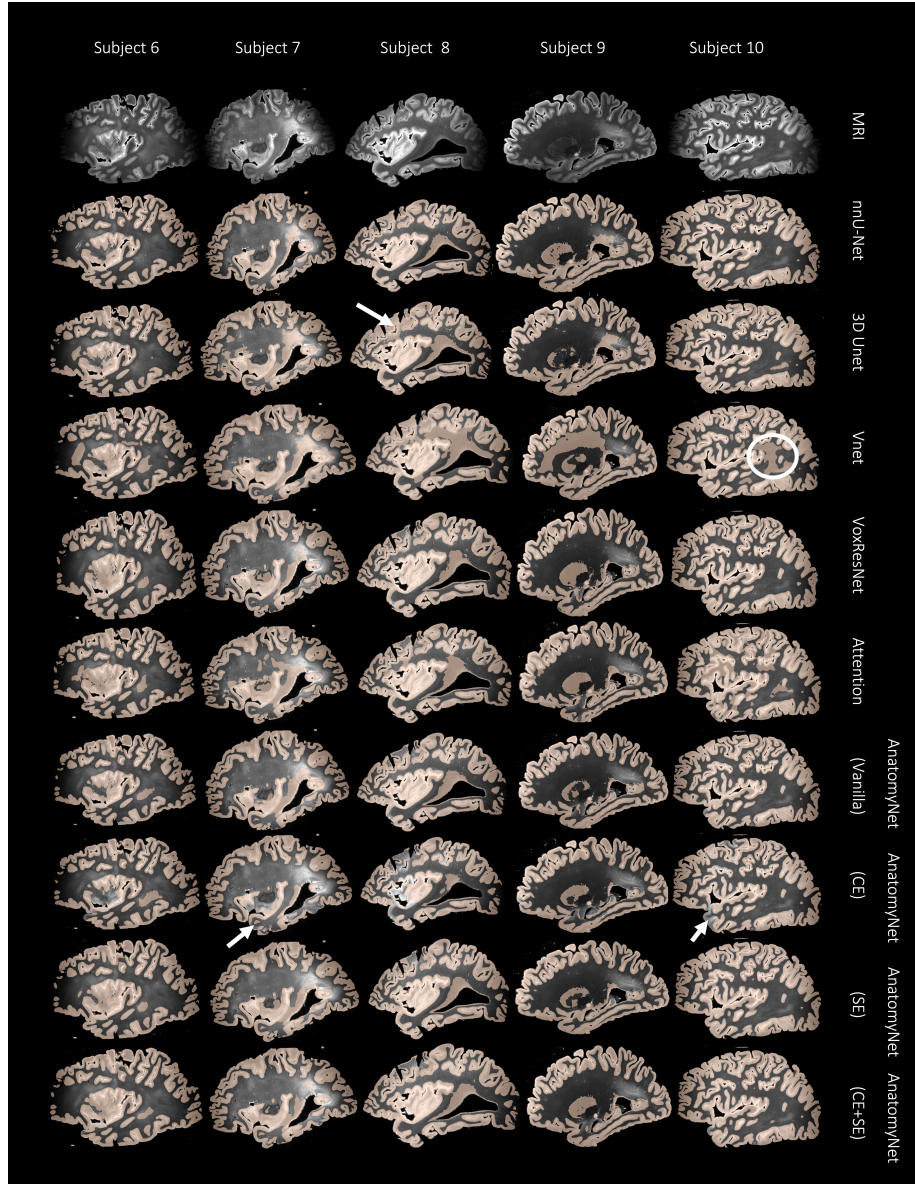


Figure 7: *Continued.* Again, notice that AnatomyNet (CE) is not able to segment certain areas in the cortical mantle (white arrows). The networks 3D Unet and Vnet oversegments the cortical mantle into the WM. nnU-Net overcomes all of these limitations.

#### 4.1.2. Intra-class correlation coefficient

We compare cortical thickness (mm) at 16 cortical landmarks between automated gray matter segmentations obtained by the nine networks and the semi-automated segmentation method, which serves as the reference standard.

Table 4.2 tabulates the Average fixed raters ICC scores for all the nine networks. We observe that the nnU-Net is the best performing segmentation model with a mean ICC of 0.72 across all the 16 cortical regions. The variants of AnatomyNet have mean ICC values of, Vanilla: 0.40, CE: 0.47, CE+SE: 0.40 and SE: 0.34. We observe that the variants of AnatomyNet were the top performing models when evaluated using DSC scores at patch-level, but did not generalize to robustly segment the entire cortical mantle; and thereby failed to show good correlation of regional cortical thickness when compared with the reference standard reference cortical thickness. The other four models also had very low ICC values: VoxResNet: 0.45, VNet: 0.28, 3D Unet: 0.47, and Attention Unet: 0.35.

In Figure 8 (A), we observe strong correlation between reference standard and automated nnU-Net segmentation-based thickness measurements for the 16 cortical landmarks. Eight out of the 16 regions were found to have correlation coefficient ( $r$ ) greater than 0.6. We also observe high ICC scores with 9 regions having ICC greater than 0.7. The Bland-Altman plots in Supplementary Figure 3 again show the strong agreement between measurements based-on manual and automated segmentations, thus confirms that automated segmentations are accurate to give desirable cortical thickness measurements.

Therefore, based on quantitative evaluation in terms of DSC and HD95 scores, ICC values, and the qualitative visual inspection of the segmentations for the nine neural network architectures, we conclude that nnU-Net is the best performing model.

#### 4.2. Other structures: Subcortical, WMH and WM segmentation

Based on the superior performance of nnU-Net, as explained in the previous section, we employ nnU-Net to perform the multi-label segmentation for

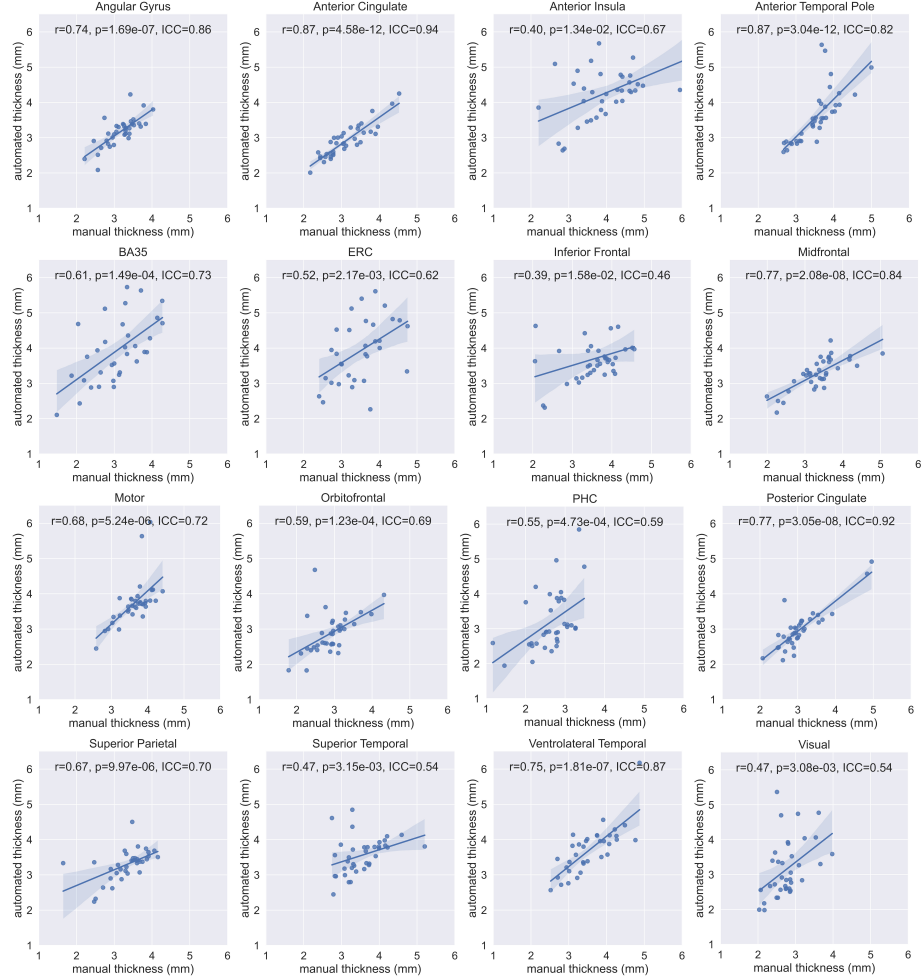


Figure 8: Regional cortical thickness measurements. (A) Figure shows correlation plots between cortical thickness measured by automated nnU-Net (y-axis) and reference standard manual segmentations (x-axis). Within each plot, we tabulate Spearman’s correlation coefficient ( $r$ ),  $p$  value, and the Average fixed raters Intra-class correlation coefficient scores. Supplementary Figure 3 shows the corresponding Bland-Altman plots.

WMH, caudate, putamen, globus pallidus, thalamus and WM. The mean DSC scores for the four subcortical structures and WMH across all leave-one-out cross-validation experiments were: WMH: 79.70 %, caudate: 88.18 %, putamen: 85.20 %, globus pallidus: 80.12 %, and the thalamus: 87.29 %. Note that currently, we do not have a large sample size to perform cross-validation evaluation on the WM, due to the time-consuming process of manually correcting the segmentations. Figures 9 and 10 show qualitative results for all the segmented structures in 2D and 3D respectively for the entire cohort in sagittal view.

Table 3: Average fixed raters Intra-class correlation coefficient (ICC) scores for the regional cortical thickness measurements between automated nnU-Net and reference standard manual segmentations for all the nine neural network architectures. Across each row, each cell is color coded with darker shades indicating higher ICC value.

ROI\Network	VoxResNet	VNet	3D Unet	Attention UNet	AnatomyNet (SE)	AnatomyNet (CE+SE)	AnatomyNet (Vanilla)	AnatomyNet (CE)	nnU-Net
Visual	0.40	0.27	0.39	0.40	0.32	0.41	0.34	0.53	0.54
Motor	0.59	0.03	0.25	0.03	0.11	0.04	0.08	0.46	0.72
Posterior cingulate	0.57	0.51	0.46	0.39	0.46	0.68	0.62	0.88	0.92
Midfrontal	0.63	0.55	0.32	0.54	0.64	0.73	0.72	0.61	0.84
Anterior cingulate	0.86	0.67	0.72	-0.12	0.34	0.56	0.51	0.70	0.94
Orbitofrontal	0.66	0.44	0.48	0.62	0.69	0.61	0.64	0.51	0.69
Superior temporal	0.52	0.27	0.44	0.34	0.34	0.35	0.38	0.30	0.54
Inferior frontal	0.13	-0.01	0.28	0.16	-0.17	-0.09	0.34	0.37	0.46
Anterior insula	-0.14	0.44	0.50	0.08	0.36	0.22	0.30	-0.16	0.67
Anterior temporal	0.53	0.28	0.52	0.58	0.24	0.12	0.20	-0.21	0.82
Ventrolateral	0.27	0.50	0.40	0.39	0.08	0.64	0.31	0.60	0.87
Superior parietal	0.78	0.46	0.48	0.46	0.81	0.71	0.81	0.82	0.70
Angular gyrus	0.39	0.22	0.25	0.25	0.33	0.26	0.45	0.44	0.86
ERC	0.27	-0.13	0.79	0.57	0.12	0.47	0.11	0.64	0.62
BA35	0.53	0.56	0.79	0.56	0.61	0.52	0.54	0.56	0.73
PHC	0.15	0.41	0.36	0.42	0.21	0.23	0.11	0.49	0.59
Mean	<b>0.45</b>	<b>0.28</b>	<b>0.47</b>	<b>0.35</b>	<b>0.34</b>	<b>0.40</b>	<b>0.40</b>	<b>0.47</b>	<b>0.72</b>

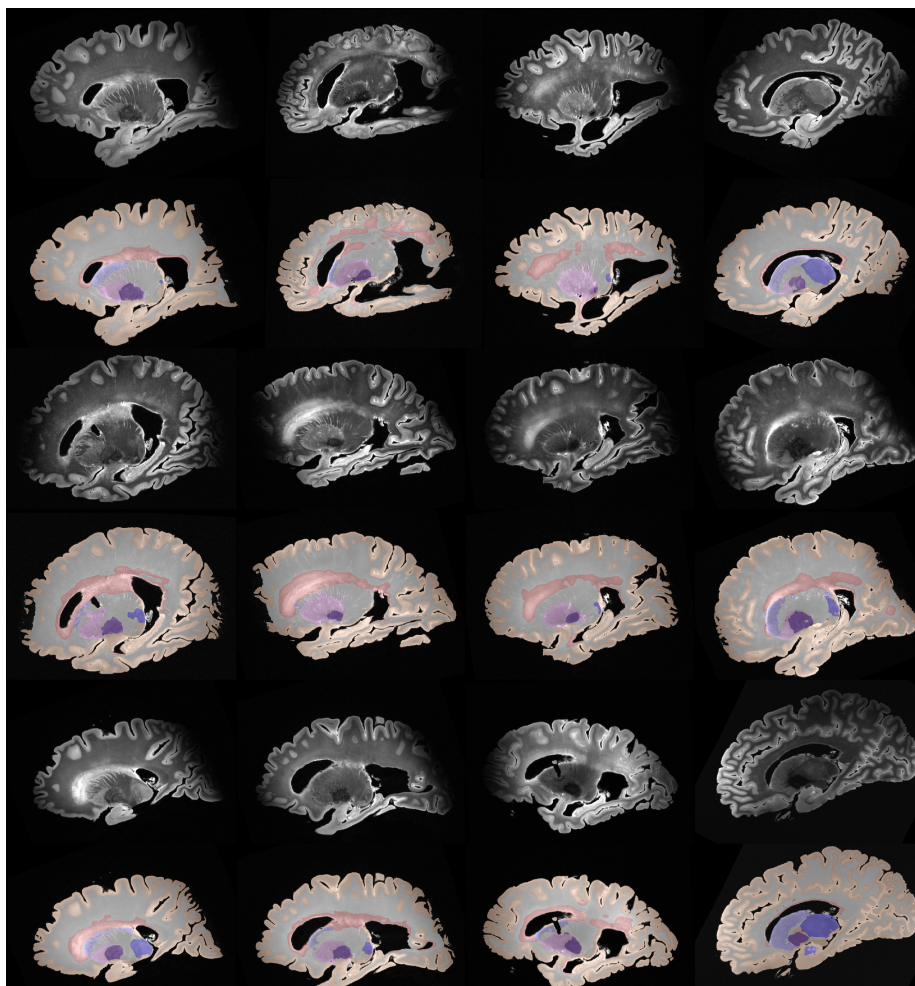


Figure 9: Automated segmentations by nnU-Net of cortical gray matter, WMH, WM and the four subcortical structures for all the 37 subjects in the cohort.

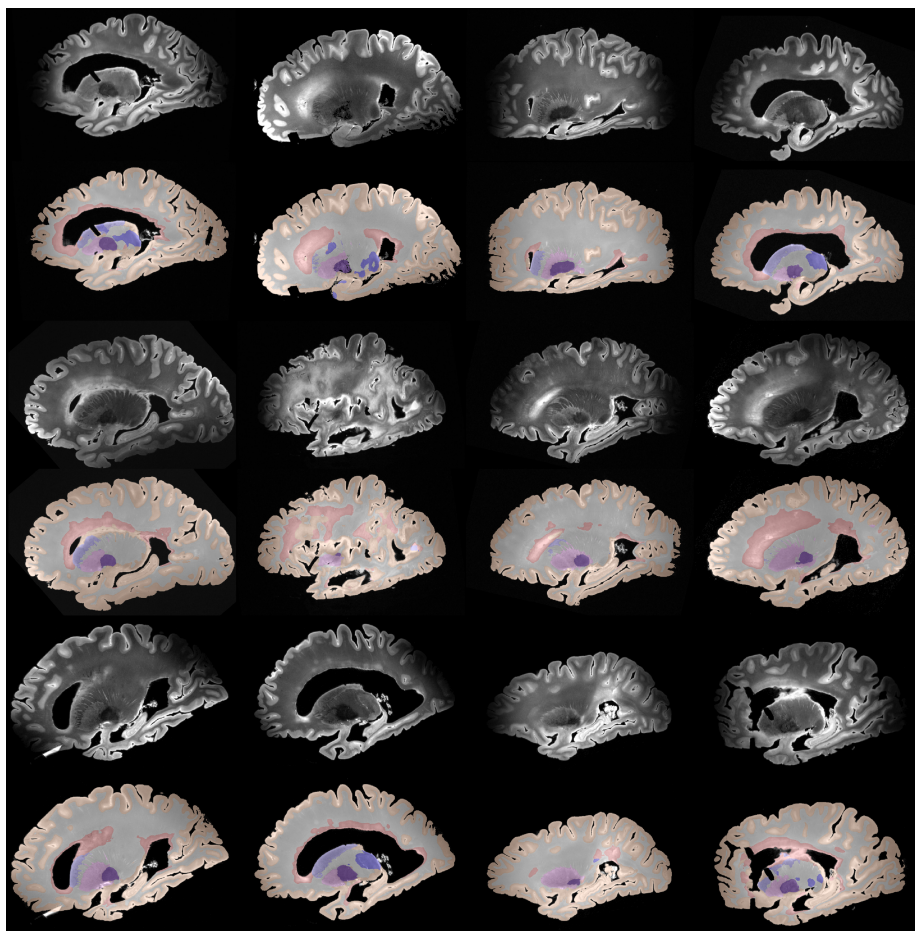


Figure 9: *Continued.* Automated segmentations by nnU-Net of cortical gray matter, WMH, WM and the four subcortical structures for all the 37 subjects in the cohort.

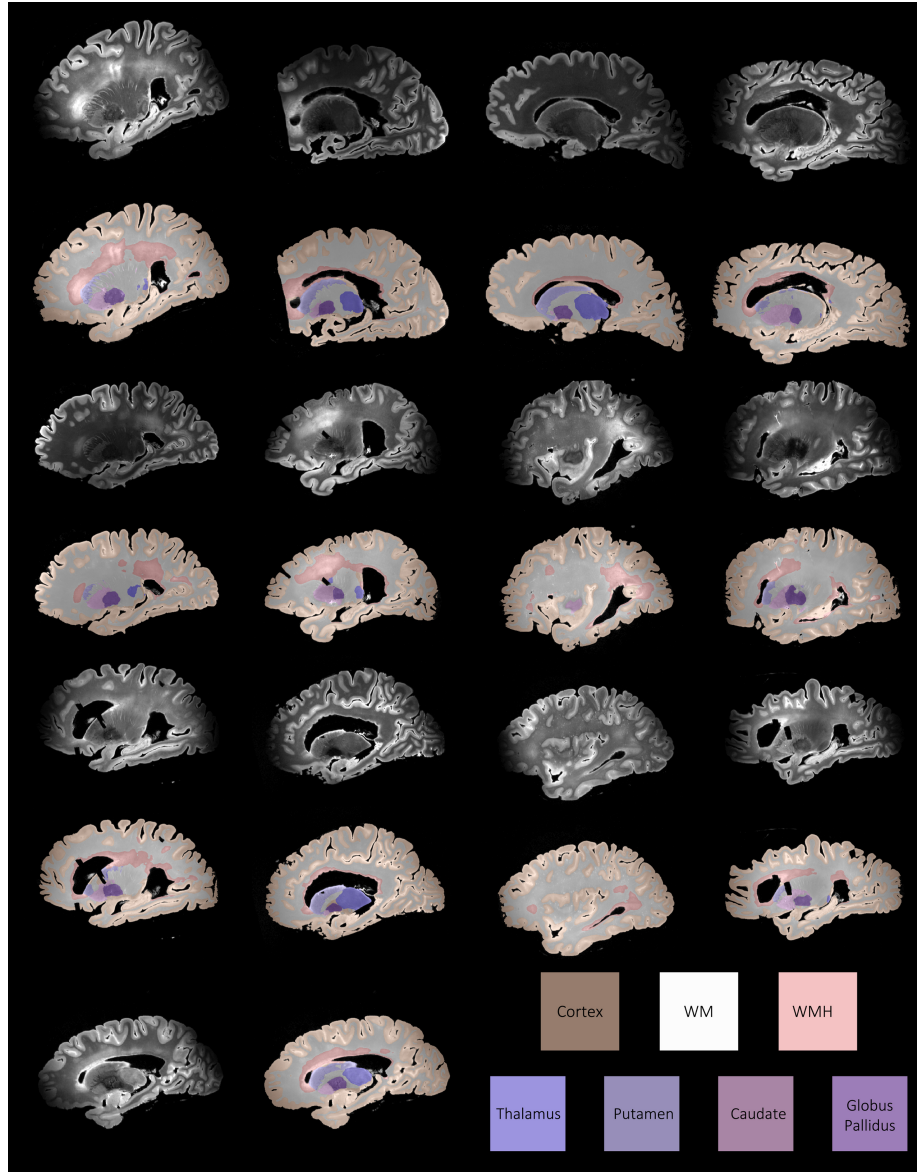


Figure 9: *Continued.* Automated segmentations by nnU-Net of cortical gray matter, WMH, WM and the four subcortical structures for all the 37 subjects in the cohort shown in sagittal view.

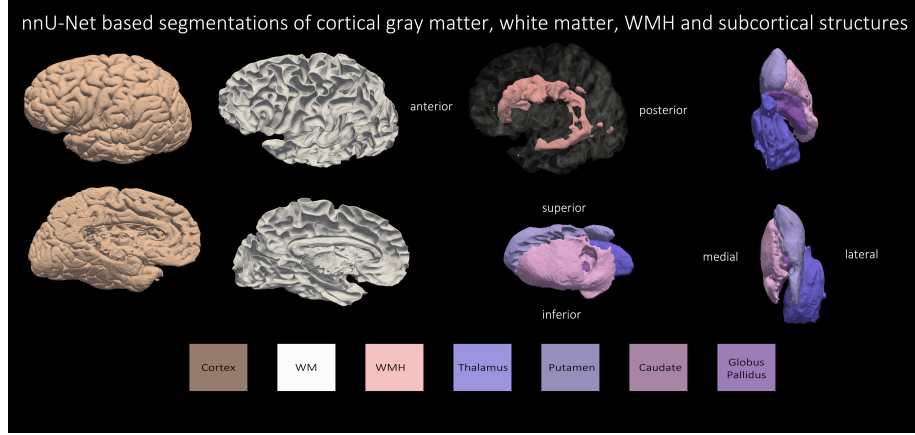


Figure 10: Three-dimensional renderings of automated segmentations by nnU-Net of cortical gray matter, WM, WMH and the four subcortical structures for the subject with Primary age-related tauopathy and Cerebrovascular disease.

#### 4.3. Generalization to other imaging sequences and protocols.

Further highlighting the strong generalization properties of nnU-Net, Figure 11 illustrates that a model trained on 7 T  $0.3 \times 0.3 \times 0.3 \text{ mm}^3$  T2w images, is able to generalize well to MRI sequences and resolutions unseen during training. Shown are the segmentation results on T2\*w gradient echo ex vivo images acquired Tisdall et al. (2021) at  $0.28 \times 0.28 \times 0.28 \text{ mm}^3$  and  $0.16 \times 0.16 \times 0.16 \text{ mm}^3$  resolution along with cortical gray matter segmentation in the publicly available ex vivo T2w image acquired at 3 T at a lower resolution of  $0.4 \times 0.4 \times 0.4 \text{ mm}^3$  Mancini et al. (2020). Currently, we are in the process of scanning the given specimens using the T2\*w sequence at  $0.28 \times 0.28 \times 0.28 \text{ mm}^3$  resolution; and hence, in future we will be able to generate segmentations on these high resolution images as well for further analyses.

#### 4.4. Morphometry associations with underlying Neuropathology

We correlate regional cortical thickness measures derived from nnU-net gray matter segmentation with corresponding regional ratings of p-tau pathology and neuronal loss density, amyloid- $\beta$  ratings, CERAD and Braak staging as ex-

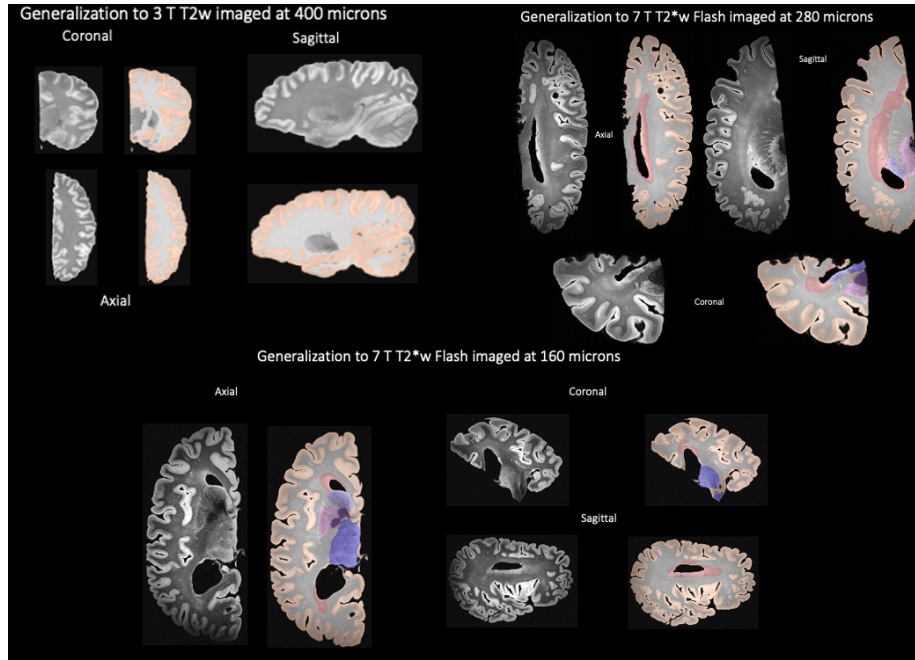


Figure 11: Generalization to other unseen imaging sequences. nnU-Net architecture trained on 7 T T2w images at  $0.3 \text{ mm}^3$  generalized well to images acquired at 3 T at lower resolution of  $0.5 \times 0.5 \times 0.5 \text{ mm}^3$  available at Mancini et al. (2020). nnU-Net architecture trained on 7 T T2w images at  $0.3 \times 0.3 \times 0.3 \text{ mm}^3$  generalized well to image acquired at 7 T at lower resolution of  $0.28 \times 0.28 \times 0.28 \text{ mm}^3$ . Shown here is a FTLD-TDP case. nnU-Net architecture trained on 7 T T2w images at  $0.3 \times 0.3 \times 0.3 \text{ mm}^3$  generalized well to images acquired at 7 T at lower resolution of  $0.16 \times 0.16 \times 0.16 \text{ mm}^3$  for a GGT (Globular glial tauopathy) case.

Table 4: Morphometry associations with underlying Neuropathology. Shown is the one-sided Spearman’s correlation, with uncorrected p-value in bracket, between regional cortical thickness measures derived from nnU-net gray matter segmentation with corresponding regional ratings of p-tau pathology and neuronal loss density, amyloid- $\beta$  ratings, CERAD score, and Braak staging and compare with those measurements based-on manual segmentations. Each cell is color coded with darker shades indicating more negative correlations. \* indicates that the test survived Benjamini Hochberg multiple testing correction Benjamini and Hochberg (1995).

Pathology ratings	Abeta		Braak stage		CERAD		p-tau		Neuronal loss	
	Manual	nnU-Net	Manual	nnU-Net	Manual	nnU-Net	Manual	nnU-Net	Manual	nnU-Net
ROI										
Visual	0.01 (0.487)	0.16 (0.241)	-0.20 (0.188)	0.02 (0.466)	0.01 (0.480)	0.14 (0.268)	-0.30 (0.085)	-0.01 (0.481)	-0.04 (0.428)	-0.08 (0.363)
Motor cortex	0.07 (0.376)	-0.29 (0.098)	0.11 (0.320)	-0.07 (0.377)	-0.18 (0.216)	-0.05 (0.409)	-	-	-	-
Posterior cingulate	-0.35 (0.054)	-0.20 (0.191)	-0.28 (0.099)	-0.03 (0.455)	-0.36 (0.050)	-0.23 (0.156)	-0.31 (0.080)	-0.13 (0.275)	-0.50 (0.009)	-0.23 (0.153)
Midfrontal	-0.40 (0.032)	-0.66 (0.0004)*	-0.24 (0.186)	-0.47 (0.013)	-0.18 (0.211)	-0.40 (0.033)	-0.26 (0.124)	-0.54 (0.005)	-0.33 (0.064)	-0.44 (0.019)
Anterior cingulate	-0.27 (0.112)	-0.35 (0.057)	-0.14 (0.263)	-0.21 (0.176)	-0.19 (0.192)	-0.18 (0.206)	0.06 (0.395)	-0.11 (0.308)	-0.23 (0.156)	-0.24 (0.136)
Orbitofrontal	0.16 (0.242)	-0.31 (0.078)	0.23 (0.155)	-0.18 (0.208)	-0.17 (0.223)	0.16 (0.236)	-	-	-	-
Superior temporal	0.11 (0.306)	0.04 (0.478)	0.16 (0.237)	0.28 (0.107)	0.11 (0.308)	0.04 (0.421)	-0.01 (0.474)	0.00 (0.497)	0.10 (0.328)	0.13 (0.292)
Inferior frontal	0.14 (0.260)	-0.51 (0.008)	0.24 (0.145)	-0.23 (0.157)	0.22 (0.161)	-0.01 (0.482)	0.19 (0.197)	-0.12 (0.294)	-0.03 (0.455)	-0.13 (0.281)
Anterior insula	-0.03 (0.450)	0.04 (0.423)	-0.22 (0.109)	0.18 (0.216)	-0.45 (0.019)	0.02 (0.471)	-0.37 (0.045)	-0.01 (0.476)	-0.53 (0.006)	0.10 (0.333)
Anterior temporal	-0.40 (0.033)	-0.30 (0.089)	-0.50 (0.008)	-0.28 (0.097)	-0.44 (0.021)	-0.29 (0.093)	-0.59 (0.002)*	-0.39 (0.036)	-0.48 (0.011)	-0.33 (0.067)
Ventrolateral temporal	-0.21 (0.180)	-0.47 (0.013)	-0.49 (0.011)	-0.29 (0.091)	-0.39 (0.040)	-0.11 (0.310)	-0.13 (0.290)	-0.11 (0.310)	-0.48 (0.016)	-0.35 (0.061)
Superior parietal	-0.07 (0.387)	-0.16 (0.245)	-0.21 (0.180)	-0.18 (0.217)	-0.36 (0.055)	-0.47 (0.016)	-0.58 (0.003)*	-0.37 (0.049)	-0.19 (0.203)	-0.04 (0.431)
Angular gyrus	-0.42 (0.026)	-0.29 (0.095)	-0.39 (0.038)	-0.20 (0.184)	-0.34 (0.060)	-0.17 (0.219)	-0.58 (0.003)*	-0.47 (0.013)	-0.51 (0.007)	-0.22 (0.164)
Entorhinal cortex	-0.25 (0.156)	-0.35 (0.069)	-0.58 (0.004)	-0.50 (0.014)	-0.40 (0.043)	-0.25 (0.152)	-0.64 (0.001)*	-0.30 (0.106)	-0.48 (0.022)	-0.51 (0.016)
Brodmann Area 35	-0.13 (0.293)	-0.12 (0.307)	-0.47 (0.016)	-0.38 (0.046)	-0.21 (0.178)	-0.16 (0.238)	-0.15 (0.264)	-0.37 (0.051)	-0.40 (0.039)	-0.48 (0.015)
Parahippocampal cortex	-0.30 (0.089)	-0.28 (0.107)	-0.41 (0.028)	-0.31 (0.079)	-0.14 (0.270)	-0.27 (0.113)	0.08 (0.361)	-0.23 (0.156)	-0.20 (0.181)	-0.31 (0.079)

plained in Section 3.4. We observe that the analysis based on manual segmentations show a similar trend as the automated segmentations, which suggests that automated segmentations obtained from the developed pipeline provide meaningful associations with underlying neuropathological measurements, and are thus reliable for validation of clinical ratings.

#### 4.4.1. Regional cortical atrophy correlation patterns with underlying ratings

Table 4.3 compares the correlation between the regional cortical thickness and the pathology ratings for measurements based-on automated nnU-Net and manual reference segmentations for the subjects within the AD continuum. For the nnU-Net segmentation-based regional cortical thickness measurements, we observe significant negative one-sided Spearman’s correlation:

- in midfrontal ( $r=-0.66$ ,  $p=0.0004$ ), inferior frontal ( $r=-0.51$ ,  $p=0.008$ ) and ventrolateral temporal cortex ( $r=-0.47$ ,  $p=0.013$ ) with amyloid- $\beta$ . Only midfrontal cortex met the more conservative Benjamini-Hochberg FDR = 0.05 threshold;
- in midfrontal ( $r=-0.47$ ,  $p=0.013$ ), entorhinal cortex ( $r=-0.50$ ,  $p=0.014$ ) and Brodmann Area 35 ( $r=-0.38$ ,  $p=0.046$ ) with Braak staging;
- in midfrontal cortex ( $r=-0.40$ ,  $p=0.033$ ), superior parietal ( $r=-0.47$ ,  $p=0.016$ ) with CERAD rating;
- in midfrontal ( $r=-0.54$ ,  $p=0.005$ ), angular gyrus ( $r=-0.47$ ,  $p=0.013$ ) in anterior temporal pole ( $r=-0.39$ ,  $p=0.036$ ), and superior parietal ( $r=-0.37$ ,  $p=0.049$ ) with p-tau rating;
- in midfrontal cortex ( $r=-0.44$ ,  $p=0.019$ ), entorhinal cortex ( $r=-0.51$ ,  $p=0.016$ ), and Brodmann Area 35 ( $r=-0.48$ ,  $p=0.015$ ) with neuronal loss rating.

#### 4.4.2. Subcortical volume differentiates diagnostic groups

Figure 12 illustrates pairwise comparisons of subcortical volumes between the five diagnostic groups as categorized into five Alzheimer’s Disease and Re-

lated Dementia (ADRD) diagnostic groups:

- Alzheimer's Disease Spectrum (N=13) including Limbic-predominant Age-related TDP-43 Encephalopathy (LATE),
- tauopathy 4-Repeat (N=5) including Progressive supranuclear palsy (PSP), Corticobasal degeneration (CBD), and Globular glial tauopathy (GGT),
- Lewy body disease (LBD) (N=8),
- Frontotemporal Lobar Degeneration with TDP inclusions (N=8),
- tauopathy miscellaneous (N=3) including Frontotemporal dementia with Parkinsonism linked to chromosome 17 (FTD-17), and unclassifiable.

We observed significant differences, which survived the multiple comparisons test using Benjamini Hochberg FDR, between:

- AD and Tau-4R ( $p<0.01$ ), AD and FTLD-TDP ( $p<0.05$ ), Tau-4R and LBD ( $p<0.05$ ), Tau-4R and Tau-Misc ( $p<0.05$ ), FTLD-TDP and Tau-Misc ( $p<0.05$ ) in caudate,
- AD and FTLD-TDP ( $p<0.001$ ), and AD and Tau-4R ( $p<0.01$ ) in putamen.

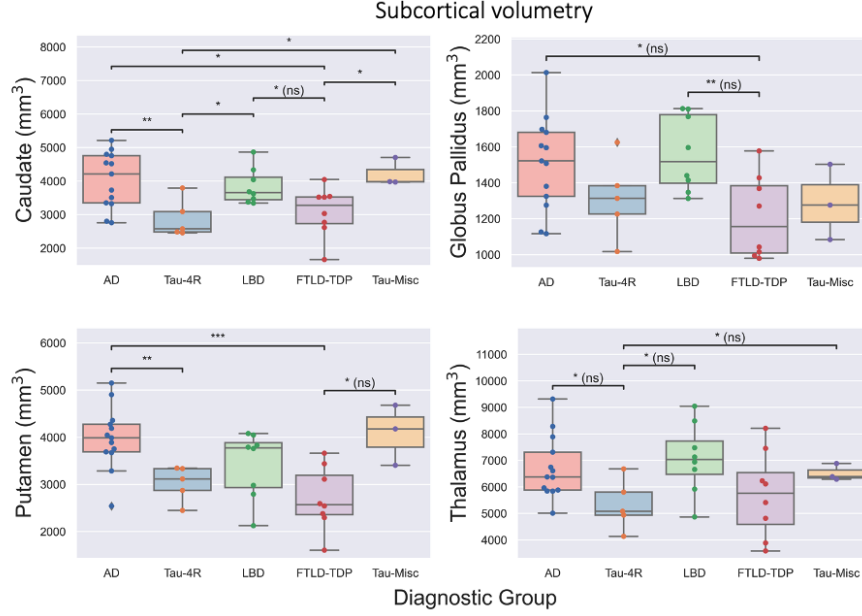


Figure 12: Pairwise comparisons of the subcortical volumes helps in differentiating AD/DRD diagnostic groups. Legend \*:  $0.01 < p \leq 0.05$ ; \*\*:  $0.001 < p \leq 0.01$ ; \*\*\*:  $0.0001 < p \leq 0.001$ . Note that 'ns' indicates that the region did not survive the more conservative Benjamini-Hochberg FDR correction.

#### 4.4.3. Normalized WMH volume correlation patterns with regional cortical thickness and subcortical volumes

Table 5 compares the correlation between the regional cortical thickness and subcortical volumes with the normalized WMH (WMH volume divided by the total WM volume) volume for measurements based-on automated nnU-Net and manual reference segmentations for all the subjects in the given cohort. For the nnU-Net segmentation-based regional thickness measurements, we observe significant negative one-sided Spearman's correlation in midfrontal cortex ( $r = -0.34$ ,  $p = 0.021$ ) and at trend-level for superior temporal pole ( $r = -0.28$ ,  $p = 0.043$ ) with normalized WMH volume. For the subcortical structures, significant negative one-sided partial Spearman's correlation was found in putamen ( $r = -0.44$ ,  $p = 0.003$ ) with normalized WMH volume after controlling for ICV.

Table 5: White matter hyperintensities volume correlations. Shown is the one-sided Spearman’s correlation, with uncorrected p-value in bracket, for correlation between normalized WMH volume (obtained by dividing the WMH volume with the corresponding WM) with regional cortical thickness based-on nnU-Net and manual segmentations. For the four subcortical structures, partial one-sided Spearman’s correlation, with uncorrected p-value in bracket is shown, controlling for intra-cranial volume. \* indicates that the test survived Benjamini Hochberg multiple testing correction. Each cell is color coded with darker shades indicating more negative correlations.

White Matter Hyperintensities (WMH)					
ROI	nnU-Net		N	Manual	
Visual	-0.24	(0.075)	37	0.04	(0.410)
Motor cortex	0.04	(0.406)	36	0.08	(0.331)
Posterior cingulate	-0.08	(0.318)	37	-0.15	(0.191)
Midfrontal	-0.34	(0.021)	37	-0.34	(0.018)
Anterior cingulate	0.03	(0.425)	37	0.00	(0.494)
Orbitofrontal	-0.20	(0.116)	37	-0.04	(0.397)
Superior temporal pole	-0.28	(0.043)	37	-0.22	(0.099)
Inferior frontal	0.06	(0.368)	37	-0.14	(0.203)
Anterior insula	-0.19	(0.125)	37	-0.22	(0.097)
Anterior temporal pole	-0.12	(0.230)	37	-0.12	(0.240)
Ventrolateral temporal cortex	-0.12	(0.248)	36	-0.33	(0.024)
Superior parietal	-0.07	(0.338)	35	-0.12	(0.249)
Angular gyrus	-0.14	(0.212)	37	-0.30	(0.037)
Entorhinal cortex	-0.16	(0.186)	32	0.26	(0.072)
Brodmann Area 35	0.02	(0.448)	33	-0.07	(0.353)
Parahippocampal cortex	0.04	(0.400)	37	-0.09	(0.295)
Caudate	-0.27	(0.059)	37	-	-
Putamen	-0.44	(0.003)*	37	-	-
Globus pallidus	-0.14	(0.201)	37	-	-
Thalamus	-0.30	(0.036)	37	-	-

## 5. Discussion

### *Segmentation pipeline*

To our knowledge, the current study is the most comprehensive assessment of automated segmentation of 7 T ex vivo human brain MRI. Our evaluation is performed in a relatively large cohort of 37 brain specimens with a range of neurodegenerative pathologies, and focuses on multiple tasks: cortical gray matter segmentation, subcortical gray matter structure segmentation, as well as white matter and WMH segmentation. For cortical segmentation, we evaluated nine deep learning architectures using direct metrics of segmentation accuracy (cross-validation DSC), derived morphological metrics (ICC of regional cortical thickness with the reference standard; comparison of associations with pathology), and visual assessment.

Our paper stands apart from recent work on automated segmentation of ex vivo brain MRI, which has either been performed in lower-resolution 3T MRI scans Mancini et al. (2020), or in smaller high-resolution datasets Jonkman et al. (2019). Mancini et al. (2020) used FreeSurfer Fischl (2012) and a Bayesian modelling technique, SAMSEG Puonti et al. (2016), to map a single post-mortem specimen imaged at 3 T but did not evaluate on higher resolution 7 T. In addition to segmenting the cortical gray matter, Mancini et al. (2020) parcellate the cortex into anatomical regions. A separate study Kotrotsou et al. (2014) also segmented the entire hemisphere but applied to a smaller dataset of 7 subjects with a slice thickness of 1.5 mm and imaged at 3 T. Both these methods relied on multi-atlas based image segmentation which is dependent on registration between high resolution ex vivo and low resolution in vivo atlases. Registration between inter-modality ex vivo and in vivo currently remains challenging, especially for higher-resolution 7T ex vivo MRI [Casamitjana et al. (2021), Casamitjana et al. (2022) and Daly et al. (2021)]. Other recent studies on ex vivo [Yushkevich et al. (2021); Wisse et al. (2021); Ravikumar et al. (2021); Adler et al. (2014, 2018); Iglesias et al. (2015); Augustinack et al. (2014); DeKraaker et al. (2018, 2021)] post-mortem human brain morphometry focused on spe-

cific areas such as the hippocampus or the medial temporal lobe, and relied on manual segmentation to guide inter-subject registration and atlas generation.

Our evaluation demonstrates that deep learning-based segmentation pipelines, particularly nnU-Net, can generate high-quality segmentations of cortical gray matter, subcortical structures, normal-appearing white matter, and white matter lesions even with very limited training data. With inference time of around 15 minutes on a CPU, our pipeline represents the first step towards fast, automated and reliable brain mapping of high resolution ex vivo whole-hemisphere MRI. Our nnU-Net based pipeline generalized well to areas of low contrast unseen during training, as well as to other MRI protocols, field strengths, and resolutions. Moreover, thickness measures derived from the deep learning-based automated segmentations concur with the reference standard, and similar associations between thickness and pathology are detected using automatically-derived and reference standard thickness measurements, albeit with the latter usually having higher effect sizes. This suggests that fully automated cortical thickness analysis is feasible for ex vivo MRI. Indeed, with further improvements to accuracy (e.g., a larger training set covering more of the hemisphere), automated ex vivo segmentation may make the labor-intensive and subjective semi-automated approach to cortical thickness measurement employed unnecessary. Thus, the study suggests the feasibility of a fully automated cortical thickness analysis in ex vivo MRI analogous to the way FreeSurfer is used for in vivo MRI morphometry, which forms the basis of our future research direction.

The limitations of the current pipeline include a relatively small training set for cortical gray matter segmentation that did not capture the whole hemisphere, and thus limited our ability to use direct metrics such as DSC to evaluate overall segmentation accuracy. Indeed, the method that performed best in terms of cross-validation DSC (AnatomyNet) performed worse in areas unseen during training than nnU-Net. To address this limitation, in future work we plan to train the method on manual segmentations of whole hemispheres; however, generating such a dataset will require a significant additional investment in

time and effort. Another key limitation is that unlike most *in vivo* pipelines (Fischl (2012)), our pipeline does not impose topological constraints on the segmentation or map the segmented cortex to an atlas/template. As a result, we still rely on manually placed landmarks to measure thickness in specific anatomical regions, and we do not show 3D maps of thickness as is common in *in vivo* morphometry studies.

Due to limited availability of reference standard segmentations, parcellating the brain into subregions, as in done in most *in vivo* MRI currently remains a challenge. We intend to address this limitation by semi-manually annotating the brain into different cortical and subcortical structures, guided by anatomical priors derived from *in vivo* MRI studies. In certain locations due to partial volume effects, the deep sulci are mis-labeled as cortical gray matter which might lead to over estimation of cortical thickness. This could be mitigated by incorporating topology correction methods for cortical and white matter surface segmentation. We could then develop techniques for groupwise normalization studies by building a template for *ex vivo* MRI. Towards this goal, we are currently developing deep learning-based methods for registration between *ex vivo* and *in vivo* MRI. Our work is limited to ADRD, but in future we plan to evaluate our methodological pipeline on a cohort of healthy control specimens obtained from a separate post-mortem *ex vivo* dataset [Jonkman et al. (2019); Frigerio et al. (2021); Boon et al. (2019)].

### ***Neuropathology associations***

With the help of the proposed segmentation and morphometry pipeline, we were able to conduct studies of *ex vivo* MRI that have not been possible before: for example, we replicated some of the findings from Sadaghiani et al. (2022) (albeit with weaker overall effect sizes), compared subcortical volume-try across different ADRD diagnostic groups, and drew associations between WMH volume, cortical thickness and subcortical volumes. Here, we discuss some of the interesting findings, recognizing that given the heterogeneity and relatively small size of the dataset, in future these would need to be replicated in

a larger dataset. Strong ex vivo image analysis frameworks allows us to better understand the distinct roles and degrees by which in vivo pathology affects neurodegeneration. Prior work shows how amyloid- $\beta$ , p-tau, TDP-43, etc have differential influences on atrophy Dugger and Dickson (2017); Robinson et al. (2018); Matej et al. (2019); Negash et al. (2011), and an automated pipeline and dataset as shown here can bolster the quantitative interrogation of these open questions. It will allow future work to study links between macro structure and other local processes beyond pathology, including inflammatory markers, gene expression, etc. We also note that measuring WMH in postmortem imaging adds value to histological studies, as we have less clear measures of vascular burden with traditional autopsy, which will allow probing of WMH for better understanding their pathologic correlates given their non-specific nature.

The current study demonstrates the associations between regional cortical thickness measurements with the underlying semi-quantitative neuropathological ratings for the AD cohort. Negative correlations between p-tau and cortical thickness were found to be significant in angular gyrus and midfrontal regions, which is in line with previous research previous in antemortem [LaPoint et al. (2017); Harrison et al. (2021); Xia et al. (2017); Das et al. (2019); Whitwell et al. (2018)] and postmortem *in situ* MRI Frigerio et al. (2021) studies. Tau pathology is concurrent with neuronal loss in ADRD Dawe et al. (2011); Ohm et al. (2021); Jack Jr et al. (2018) and the loss of neurons is likely a key source of cortical atrophy. We observed that cortical thickness showed significant negative correlation with neuronal loss in BA35 and entorhinal cortex, regions where p-tau pathology have predicted the atrophy rate LaPoint et al. (2017); Xie et al. (2018); La Joie et al. (2020) in in vivo studies. Significant negative correlations were observed between Braak staging and cortical thickness in midfrontal, ERC and BA35, regions consistent with high p-tau uptake in positron emission tomography (PET) imaging with cortical thickness on MRI. Tau pathology in Braak regions play an important role in cortical atrophy and cognitive decline during the course of AD. Similar findings reported for global cortical thickness with *in situ* post-mortem MRI in Frigerio et al. (2021). The relationship between

amyloid- $\beta$  and neurodegeneration is thought to be rather indirect Jack Jr et al. (2018); Gómez-Isla and Frosch (2022). Nevertheless, we did find strong negative correlations in between thickness and amyloid- $\beta$  in midfrontal, inferior frontal, and ventrolateral temporal cortex, brain regions implicated in working memory capacity Barbey et al. (2013); Chiou and Ralph (2018). Our observation of a significant negative correlation of CERAD scores with cortical thickness in the superior parietal region is consistent with previous studies relating CERAD with cortical thickness Santos et al. (2011); Paaanen et al. (2013).

Next, the volumetry of the subcortical structures helped distinguish subjects based on their diagnostic grouping within the ADRD spectrum. We found that caudate and putamen significantly atrophied in FTLD than in AD, which is line with a previous study Möller et al. (2015) which showed that bvFTD patients had significantly more atrophy in caudate nucleus than AD patients. Caudate and putamen are affected in both behavioural and language phenotypes of FTD and along with globus pallidus is known to be smaller than controls Halabi et al. (2013); Landin-Romero et al. (2017); Watanabe et al. (2018); Bocchetta et al. (2021); Dutt et al. (2016); Miletić et al. (2022); and post mortem volumetry has confirmed atrophy in the anterior thalamus and a reduction for bvFTD with TDP-43 (Rohrer et al. (2015)). We obtain similar trends of decreased volume of globus pallidus and thalamus for FTLD-TDP than AD.

Lastly, WMH have been implicated in age-related cognitive decline and AD, which is characterized by atrophy in the cortical mantle and the MTL [Rizvi et al. (2018); Du et al. (2005); Dadar et al. (2022)]. In our study, we observed significant negative correlations between normalized WMH and thickness in midfrontal and superior temporal regions. Previous work Reijmer et al. (2015) showed that the disruption of structural and functional connectivity has an impact on executive functioning and memory among individuals with high WMH volume. To this point, our study found that subcortical atrophy was significantly negatively correlated with WMH volume in putamen and thalamus suggesting more global effects on brain volume.

A limitation of our study borne out of the exclusion of hemispheres with sig-

nificant involvement with any other type of tauopathy or FTLT-TDP except AD for the analysis of correlations of regional cortical thickness with the underlying neuropathological ratings. Amongst the 37 specimens, 22 had AD pathology with existence of co-pathologies. Future studies may apply this dataset and pipeline to help disentangle the differential contributions of unique pathologies to individual atrophy patterns. Separately, we are aware that the pathology measures and MRI segmentation-based measures were obtained from contralateral hemispheres, which could potentially weaken the observed associations. But pathology in AD is usually largely symmetrical between the hemispheres, and therefore leaves less room for biases in the observed correlations, as claimed in a recent study Ravikumar et al. (2021) which showed that correlations between MTL thickness maps and both contralateral and ipsilateral semi-quantitative p-tau pathology scores did not detect substantially different correlation patterns. Another limitation is that our study relies on semi-quantitative measures of neuropathology, which are subjective and might not reflect a linear pathology burden. We are currently in the process of obtaining neuropathology measurements from the same hemisphere histology, and developing machine learning-based quantitative pathological ratings to further validate our work. The current study provides support for future work to use larger datasets, quantitative pathology measures to describe the contribution of multiple pathologies to brain morphology in neurodegenerative diseases. But, overall we observe a similar trend as described in our recent work Sadaghiani et al. (2022), which looked at regional cortical thickness with tau burden. These limitations could be avoided by expanding our analysis to a larger dataset, which we are actively working towards.

## ***Conclusion***

While there is increased interest in using high-resolution ex vivo MRI of the human brain for discovering associations between brain structure and pathology, automated tools for the analysis of such complex images have received much less attention compared to *in vivo* MRI. Our study used a relatively large dataset

of 37 high resolution T2w 7 T ex vivo whole-hemisphere MRI scans to evaluate multiple deep learning image segmentation architectures and to develop an automatic segmentation pipeline that labels cortical gray matter, four subcortical structures (caudate, globus pallidus, putamen, and thalamus), WMH, and normal-appearing white matter. We report good agreement between thickness measures derived from our deep learning pipeline with the reference standard of semi-automated thickness measurement. Our analysis linking morphometry measures and pathology demonstrated that automated analysis of ex vivo MRI yields similar findings to a labor-intensive semi-automated approach, and more broadly, that automated segmentation of *ex vivo* MRI can complement and inform *in vivo* neuroimaging in neurodegenerative diseases. We have released our pipeline as a stand-alone containerized tool that can be readily applied to other ex vivo brain datasets.

## Acknowledgments

We gratefully acknowledge the tissue donors and their families. We also thank all the staff at the Center for Neurodegenerative Research (University of Pennsylvania) for performing the autopsies and making the tissue available for this project.

## Ethics approval and consent to participate

Human brain specimens were obtained in accordance with local laws and regulations, and includes informed consent from next of kin at time of death or where possible, pre-consent during life.

## Funding

This work was supported in part by the National Institute of Health Grants: P30 AG072979, R01 AG056014, RF1 AG069474, R01 AG054519, P01 AG017586, U19 AG062418.

### Availability of data and materials

We have provided the code, scripts and Jupyter notebooks to reproduce the findings of this study at the **this** GitHub repository. The MRI data will be available upon request due to compliance and ethical issues.

### Consent for publication

All authors have reviewed the contents of the manuscript being submitted, approved of its contents and validated the accuracy of the data and consented to publication.

### Competing interests

D.A.W has received grant support from Merck, Biogen, and Eli Lilly/Avid. D.A.W received consultation fees from Neuronix, Eli Lilly, and Qynaps and is on the Data and Safety Monitoring Board for a clinical trial run by Functional Neuromodulation. J.Q.T. received revenue from the sale of Avid to Eli Lilly as co-inventor on imaging-related patents submitted by the University of Pennsylvania. D.J.I. is member of science advisory board of Denali Therapeutics. S.R.D. received consultation fees from Rancho Biosciences and Nia Therapeutics. The other authors have nothing to disclose.

### CRediT authorship contribution statement

**Pulkit Khandelwal:** Conceptualization, Data curation, Formal analysis, Investigation, Methodology, Project administration, Resources, Software, Supervision, Validation, Visualization, Roles/Writing - original draft, Writing - review and editing. **Michael Tran Duong:** Conceptualization, Data curation, Formal analysis, Investigation, Methodology, Validation, Writing - review and editing. **Shokufeh Sadaghiani:** Conceptualization, Data curation, Resources, Methodology. **Sydney Lim:** Data curation, Resources, Methodology. **Amanda Denning:** Data curation, Resources, Methodology. **Eu-**

**nice Chung:** Data curation, Resources, Methodology. **Sadhana Ravikumar:** Conceptualization, Validation, Writing - review and editing. **Sanaz Arezoumandan:** Data curation, Resources. **Claire Peterson:** Data curation, Resources. **Madigan Bedard:** Data curation, Resources. **Noah Capp:** Data curation, Resources,. Software. **Ranjit Ittyerah:** Data curation, Resources. **Elyse Migdal:** Data curation, Resources, Methodology. **Grace Choi:** Data curation, Resources, Methodology. **Emily Kopp:** Data curation, Resources, Methodology. **Bridget Loja:** Data curation, Resources, Methodology. **Eusha Hasan:** Data curation, Resources, Methodology. **Jiacheng Li:** Data curation, Resources, Methodology. **Karthik Prabhakaran:** Data curation, Resources. **Gabor Mizsei:** Data curation, Resources. **Marianna Gabrielyan:** Data curation, Resources. **Theresa Schuck:** Data curation, Resources. **Winifred Trotman:** Data curation, Project administration, Resources. **John Robinson:** Data curation, Resources. **Daniel Ohm:** Data curation, Resources, Project administration. **Edward B. Lee:** Data curation, Funding acquisition, Investigation, Project administration, Resources, Writing - review and editing. **John Q. Trojanowski:** Data curation, Project administration, Resources, Funding acquisition. **Corey McMillan:** Data curation, Resources, Funding acquisition. **Murray Grossman:** Conceptualization, Data curation, Funding acquisition. **David J. Irwin:** Data curation, Project administration, Resources, Funding acquisition, Validation, Writing - review and editing. **John Detre:** Data curation, Project administration, Resources, Validation, Writing - review and editing. **M. Dylan Tisdall:** Data curation, Project administration, Resources, Validation, Writing - review and editing. **Sandhitsu R. Das:** Conceptualization, Data curation, Formal analysis, Investigation, Methodology, Project administration, Resources, Supervision, Validation, Writing - review and editing. **Laura E.M. Wisse:** Conceptualization, Data curation, Formal analysis, Investigation, Methodology, Project administration, Resources, Supervision, Validation, Writing - review and editing. **David A. Wolk:** Conceptualization, Data curation, Funding acquisition, Investigation, Methodology, Project administration, Resources, Software, Supervision,

Validation, Visualization, Roles/Writing - original draft, Writing - review and editing. **Paul A. Yushkevich:** Conceptualization, Data curation, Formal analysis, Funding acquisition, Investigation, Methodology, Project administration, Resources, Software, Supervision, Validation, Writing - review and editing.

## References

- Adler, D.H., Pluta, J., Kadivar, S., Craige, C., Gee, J.C., Avants, B.B., Yushkevich, P.A., 2014. Histology-derived volumetric annotation of the human hippocampal subfields in postmortem mri. *Neuroimage* 84, 505–523.
- Adler, D.H., Wisse, L.E., Ittyerah, R., Pluta, J.B., Ding, S.L., Xie, L., Wang, J., Kadivar, S., Robinson, J.L., Schuck, T., et al., 2018. Characterizing the human hippocampus in aging and alzheimer’s disease using a computational atlas derived from ex vivo mri and histology. *Proceedings of the National Academy of Sciences* 115, 4252–4257.
- Alkemade, A., Bazin, P.L., Balesar, R., Pine, K., Kirilina, E., Möller, H.E., Trampel, R., Kros, J.M., Keuken, M.C., Bleys, R.L., et al., 2022. A unified 3d map of microscopic architecture and mri of the human brain. *Science advances* 8, eabj7892.
- Amunts, K., Mohlberg, H., Bludau, S., Zilles, K., 2020. Julich-brain: A 3d probabilistic atlas of the human brain’s cytoarchitecture. *Science* 369, 988–992.
- Arezoumandan, S., Xie, S.X., Cousins, K.A., Mechanic-Hamilton, D.J., Peterson, C.S., Huang, C.Y., Ohm, D.T., Ittyerah, R., McMillan, C.T., Wolk, D.A., et al., 2022. Regional distribution and maturation of tau pathology among phenotypic variants of alzheimer’s disease. *Acta Neuropathologica* , 1–14.
- Augustinack, J.C., Helmer, K., Huber, K.E., Kakunoori, S., Zöllei, L., Fischl, B., 2010. Direct visualization of the perforant pathway in the human brain with ex vivo diffusion tensor imaging. *Frontiers in human neuroscience* , 42.

- Augustinack, J.C., van der Kouwe, A.J., Fischl, B., 2013. Medial temporal cortices in ex vivo magnetic resonance imaging. *Journal of Comparative Neurology* 521, 4177–4188.
- Augustinack, J.C., Magnain, C., Reuter, M., van der Kouwe, A.J., Boas, D., Fischl, B., 2014. Mri parcellation of ex vivo medial temporal lobe. *Neuroimage* 93, 252–259.
- Barbey, A.K., Koenigs, M., Grafman, J., 2013. Dorsolateral prefrontal contributions to human working memory. *cortex* 49, 1195–1205.
- Beaujoin, J., Palomero-Gallagher, N., Boumezbeur, F., Axer, M., Bernard, J., Poupon, F., Schmitz, D., Mangin, J.F., Poupon, C., 2018. Post-mortem inference of the human hippocampal connectivity and microstructure using ultra-high field diffusion mri at 11.7 t. *Brain Structure and Function* 223, 2157–2179.
- Benjamini, Y., Hochberg, Y., 1995. Controlling the false discovery rate: a practical and powerful approach to multiple testing. *Journal of the Royal statistical society: series B (Methodological)* 57, 289–300.
- Bocchetta, M., Malpetti, M., Todd, E.G., Rowe, J.B., Rohrer, J.D., 2021. Looking beneath the surface: the importance of subcortical structures in frontotemporal dementia. *Brain Communications* 3, fcab158.
- Boon, B.D., Pouwels, P.J., Jonkman, L.E., Keijzer, M.J., Preziosa, P., van de Berg, W.D., Geurts, J.J., Scheltens, P., Barkhof, F., Rozemuller, A.J., et al., 2019. Can post-mortem mri be used as a proxy for in-vivo? a case study. *Brain communications* .
- Bulk, M., Abdelmoula, W.M., Geut, H., Wiarda, W., Ronen, I., Dijkstra, J., van der Weerd, L., 2020. Quantitative mri and laser ablation-inductively coupled plasma-mass spectrometry imaging of iron in the frontal cortex of healthy controls and alzheimer’s disease patients. *Neuroimage* 215, 116808.

- Casamitjana, A., Lorenzi, M., Ferraris, S., Peter, L., Modat, M., Stevens, A., Fischl, B., Vercauteren, T., Iglesias, J.E., 2022. Robust joint registration of multiple stains and mri for multimodal 3d histology reconstruction: Application to the allen human brain atlas. *Medical image analysis* 75, 102265.
- Casamitjana, A., Mancini, M., Iglesias, J.E., 2021. Synth-by-reg (sbr): Contrastive learning for synthesis-based registration of paired images, in: *International Workshop on Simulation and Synthesis in Medical Imaging*, Springer. pp. 44–54.
- Chen, H., Dou, Q., Yu, L., Qin, J., Heng, P.A., 2018. Voxresnet: Deep voxelwise residual networks for brain segmentation from 3d mr images. *NeuroImage* 170, 446–455.
- Chiou, R., Ralph, M.A.L., 2018. The anterior-ventrolateral temporal lobe contributes to boosting visual working memory capacity for items carrying semantic information. *NeuroImage* 169, 453–461.
- Dadar, M., Manera, A.L., Ducharme, S., Collins, D.L., 2022. White matter hyperintensities are associated with grey matter atrophy and cognitive decline in alzheimer’s disease and frontotemporal dementia. *Neurobiology of aging* 111, 54–63.
- Daly, A.C., Geras, K.J., Bonneau, R., 2021. A convolutional neural network for common coordinate registration of high-resolution histology images. *Bioinformatics* 37, 4216–4226.
- Das, S.R., Xie, L., Wisse, L.E., Vergnet, N., Ittyerah, R., Cui, S., Yushkevich, P.A., Wolk, D.A., Initiative, A.D.N., et al., 2019. In vivo measures of tau burden are associated with atrophy in early braak stage medial temporal lobe regions in amyloid-negative individuals. *Alzheimer’s & Dementia* 15, 1286–1295.
- Dawe, R.J., Bennett, D.A., Schneider, J.A., Arfanakis, K., 2011. Neuropatho-

- logic correlates of hippocampal atrophy in the elderly: a clinical, pathologic, postmortem mri study. *PloS one* 6, e26286.
- DeKraker, J., Ferko, K.M., Lau, J.C., Köhler, S., Khan, A.R., 2018. Unfolding the hippocampus: An intrinsic coordinate system for subfield segmentations and quantitative mapping. *Neuroimage* 167, 408–418.
- DeKraker, J., Köhler, S., Khan, A.R., 2021. Surface-based hippocampal subfield segmentation. *Trends in neurosciences* 44, 856–863.
- Du, A.T., Schuff, N., Chao, L.L., Kornak, J., Ezekiel, F., Jagust, W.J., Kramer, J.H., Reed, B.R., Miller, B.L., Norman, D., et al., 2005. White matter lesions are associated with cortical atrophy more than entorhinal and hippocampal atrophy. *Neurobiology of aging* 26, 553–559.
- Dugger, B.N., Dickson, D.W., 2017. Pathology of neurodegenerative diseases. *Cold Spring Harbor perspectives in biology* 9, a028035.
- Dutt, S., Binney, R.J., Heuer, H.W., Luong, P., Attygalle, S., Bhatt, P., Marx, G.A., Elofson, J., Tartaglia, M.C., Litvan, I., et al., 2016. Progression of brain atrophy in psp and cbs over 6 months and 1 year. *Neurology* 87.
- van Dyck, C.H., Swanson, C.J., Aisen, P., Bateman, R.J., Chen, C., Gee, M., Kanekiyo, M., Li, D., Reyderman, L., Cohen, S., et al., 2022. Lecanemab in early alzheimer’s disease. *New England Journal of Medicine* .
- Eckermann, M., Schmitzer, B., van der Meer, F., Franz, J., Hansen, O., Stadelmann, C., Salditt, T., 2021. Three-dimensional virtual histology of the human hippocampus based on phase-contrast computed tomography. *Proceedings of the National Academy of Sciences* 118, e2113835118.
- Edlow, B.L., Mareyam, A., Horn, A., Polimeni, J.R., Witzel, T., Tisdall, M.D., Augustinack, J.C., Stockmann, J.P., Diamond, B.R., Stevens, A., et al., 2019. 7 tesla mri of the ex vivo human brain at 100 micron resolution. *Scientific data* 6, 1–10.

- Fischl, B., 2012. Freesurfer. *Neuroimage* 62, 774–781.
- de Flores, R., Wisse, L.E., Das, S.R., Xie, L., McMillan, C.T., Trojanowski, J.Q., Robinson, J.L., Grossman, M., Lee, E., Irwin, D.J., et al., 2020. Contribution of mixed pathology to medial temporal lobe atrophy in alzheimer’s disease. *Alzheimer’s & Dementia* 16, 843–852.
- Frigerio, I., Boon, B.D., Lin, C.P., Galis-de Graaf, Y., Bol, J., Preziosa, P., Twisk, J., Barkhof, F., Hoozemans, J.J., Bouwman, F.H., et al., 2021. Amyloid- $\beta$ , p-tau and reactive microglia are pathological correlates of mri cortical atrophy in alzheimer’s disease. *Brain communications* 3, fcab281.
- García-Cabezas, M.Á., Hacker, J.L., Zikopoulos, B., 2020. A protocol for cortical type analysis of the human neocortex applied on histological samples, the atlas of von economo and koskinas, and magnetic resonance imaging. *Frontiers in Neuroanatomy* 14, 576015.
- Gómez-Isla, T., Frosch, M.P., 2022. Lesions without symptoms: understanding resilience to alzheimer disease neuropathological changes. *Nature Reviews Neurology* 18, 323–332.
- Gordon, E., Rohrer, J.D., Fox, N.C., 2016. Advances in neuroimaging in frontotemporal dementia. *Journal of Neurochemistry* 138, 193–210.
- Halabi, C., Halabi, A., Dean, D.L., Wang, P.N., Boxer, A.L., Trojanowski, J.Q., DeArmond, S.J., Miller, B.L., Kramer, J.H., Seeley, W.W., 2013. Patterns of striatal degeneration in frontotemporal dementia. *Alzheimer disease and associated disorders* 27, 74.
- Harrison, T.M., Du, R., Klencklen, G., Baker, S.L., Jagust, W.J., 2021. Distinct effects of beta-amyloid and tau on cortical thickness in cognitively healthy older adults. *Alzheimer’s & dementia* 17, 1085–1096.
- Henschel, L., Conjeti, S., Estrada, S., Diers, K., Fischl, B., Reuter, M., 2020. FastSurfer-a fast and accurate deep learning based neuroimaging pipeline. *NeuroImage* 219, 117012.

- Hyman, B.T., Phelps, C.H., Beach, T.G., Bigio, E.H., Cairns, N.J., Carrillo, M.C., Dickson, D.W., Duyckaerts, C., Frosch, M.P., Masliah, E., et al., 2012. National institute on aging–alzheimer’s association guidelines for the neuropathologic assessment of alzheimer’s disease. *Alzheimer’s & dementia* 8, 1–13.
- Iglesias, J.E., Augustinack, J.C., Nguyen, K., Player, C.M., Player, A., Wright, M., Roy, N., Frosch, M.P., McKee, A.C., Wald, L.L., et al., 2015. A computational atlas of the hippocampal formation using ex vivo, ultra-high resolution mri: application to adaptive segmentation of in vivo mri. *Neuroimage* 115, 117–137.
- Iglesias, J.E., Insausti, R., Lerma-Usabiaga, G., Bocchetta, M., Van Leemput, K., Greve, D.N., Van der Kouwe, A., Fischl, B., Caballero-Gaudes, C., Paz-Alonso, P.M., et al., 2018. A probabilistic atlas of the human thalamic nuclei combining ex vivo mri and histology. *Neuroimage* 183, 314–326.
- Irwin, D.J., 2016. Progressive supranuclear palsy, corticobasal syndrome, and other tauopathies. *International Neurology* , 157–160.
- Irwin, D.J., Cairns, N.J., Grossman, M., McMillan, C.T., Lee, E.B., Van Deerlin, V.M., Lee, V.M.Y., Trojanowski, J.Q., 2015. Frontotemporal lobar degeneration: defining phenotypic diversity through personalized medicine. *Acta neuropathologica* 129, 469–491.
- Isensee, F., Jaeger, P.F., Kohl, S.A., Petersen, J., Maier-Hein, K.H., 2021. nnu-net: a self-configuring method for deep learning-based biomedical image segmentation. *Nature methods* 18, 203–211.
- Jack Jr, C.R., Bennett, D.A., Blennow, K., Carrillo, M.C., Dunn, B., Haeberlein, S.B., Holtzman, D.M., Jagust, W., Jessen, F., Karlawish, J., et al., 2018. Nia-aa research framework: toward a biological definition of alzheimer’s disease. *Alzheimer’s & Dementia* 14, 535–562.

- Jonkman, L.E., Galis-de Graaf, Y., Bulk, M., Kaaij, E., Pouwels, P.J., Barkhof, F., Rozemuller, A.J., van der Weerd, L., Geurts, J.J., van de Berg, W.D., 2019. Normal aging brain collection amsterdam (nabca): A comprehensive collection of postmortem high-field imaging, neuropathological and morphometric datasets of non-neurological controls. *NeuroImage: Clinical* 22, 101698.
- Kenkhuis, B., Jonkman, L.E., Bulk, M., Buijs, M., Boon, B.D., Bouwman, F.H., Geurts, J.J., van de Berg, W.D., van der Weerd, L., 2019. 7t mri allows detection of disturbed cortical lamination of the medial temporal lobe in patients with alzheimer’s disease. *NeuroImage: Clinical* 21, 101665.
- Khandelwal, P., Duong, M.T., Chung, E., Sadaghiani, S., Lim, S.A., Ravikumar, S., Arezoumandan, S., Peterson, C., Bedard, M.L., Capp, N., Ittyerah, R., Migdal, E., Choi, G., Kopp, E., Patino, B.L., Hasan, E., Li, J., Prabhakaran, K., Mizsei, G., Gabrielyan, M., Schuck, T., Robinson, J.L., Ohm, D.T., Nasrallah, I.M., Lee, E.B., Trojanowski, J.Q., McMillan, C.T., Grossman, M., Irwin, D.J., Tisdall, D.M., Das, S.R., Wisse, L.E., Wolk, D.A., Yushkevich, P.A., 2022a. Deep learning for ultra high resolution t2-weighted 7 tesla ex vivo magnetic resonance imaging reveals differential subcortical atrophy across neurodegenerative diseases. *Alzheimer’s & Dementia* 18, e062628.
- Khandelwal, P., Sadaghiani, S., Chung, E., Lim, S.A., Duong, M.T., Ravikumar, S., Arezoumandan, S., Peterson, C., Bedard, M.L., Capp, N., Ittyerah, R., Migdal, E., Choi, G., Kopp, E., Patino, B.L., Hasan, E., Li, J., Prabhakaran, K., Mizsei, G., Gabrielyan, M., Schuck, T., Robinson, J., Ohm, D.T., Lee, E.B., Trojanowski, J.Q., McMillan, C.T., Grossman, M., Irwin, D.J., Tisdall, D.M., Das, S.R., Wisse, L.E., Wolk, D.A., Yushkevich, P.A., 2022b. Deep learning pipeline for cortical gray matter segmentation and thickness analysis in ultra high resolution t2w 7 tesla ex vivo mri across neurodegenerative diseases reveals associations with underlying neuropathology. *Alzheimer’s & Dementia* 18, e065737.
- Khandelwal, P., Sadaghiani, S., Ravikumar, S., Lim, S., Arezoumandan, S.,

- Peterson, C., Chung, E., Bedard, M., Capp, N., Ittyerah, R., et al., 2021. Gray matter segmentation in ultra high resolution 7 tesla ex vivo t2w mri of human brain hemispheres. *arXiv preprint arXiv:2110.07711* .
- Khandelwal, P., Yushkevich, P., 2020. Domain generalizer: A few-shot meta learning framework for domain generalization in medical imaging, in: *Domain Adaptation and Representation Transfer, and Distributed and Collaborative Learning*. Springer, pp. 73–84.
- Kiwitz, K., Schiffer, C., Spitzer, H., Dickscheid, T., Amunts, K., 2020. Deep learning networks reflect cytoarchitectonic features used in brain mapping. *Scientific Reports* 10, 1–15.
- Kotrotsou, A., Bennett, D.A., Schneider, J.A., Dawe, R.J., Golak, T., Leurgans, S.E., Yu, L., Arfanakis, K., 2014. Ex vivo mr volumetry of human brain hemispheres. *Magnetic resonance in medicine* 71, 364–374.
- La Joie, R., Visani, A.V., Baker, S.L., Brown, J.A., Bourakova, V., Cha, J., Chaudhary, K., Edwards, L., Iaccarino, L., Janabi, M., et al., 2020. Prospective longitudinal atrophy in alzheimer’s disease correlates with the intensity and topography of baseline tau-pet. *Science translational medicine* 12, eaau5732.
- Landin-Romero, R., Kumfor, F., Leyton, C.E., Irish, M., Hodges, J.R., Piguet, O., 2017. Disease-specific patterns of cortical and subcortical degeneration in a longitudinal study of alzheimer’s disease and behavioural-variant frontotemporal dementia. *Neuroimage* 151, 72–80.
- LaPoint, M.R., Chhatwal, J.P., Sepulcre, J., Johnson, K.A., Sperling, R.A., Schultz, A.P., 2017. The association between tau pet and retrospective cortical thinning in clinically normal elderly. *Neuroimage* 157, 612–622.
- Mackenzie, I.R., Neumann, M., Baborie, A., Sampathu, D.M., Du Plessis, D., Jaros, E., Perry, R.H., Trojanowski, J.Q., Mann, D., Lee, V.M., 2011. A har-

- monized classification system for ftld-tdp pathology. *Acta neuropathologica* 122, 111–113.
- Makinejad, N., Schneider, J.A., Yu, J., Leurgans, S.E., Kotrotsou, A., Evia, A.M., Bennett, D.A., Arfanakis, K., 2019. Associations of amygdala volume and shape with transactive response dna-binding protein 43 (tdp-43) pathology in a community cohort of older adults. *Neurobiology of aging* 77, 104–111.
- Mancini, M., Casamitjana, A., Peter, L., Robinson, E., Crampsie, S., Thomas, D.L., Holton, J.L., Jaunmuktane, Z., Iglesias, J.E., 2020. A multimodal computational pipeline for 3d histology of the human brain. *Scientific reports* 10, 1–21.
- Matej, R., Tesar, A., Rusina, R., 2019. Alzheimer’s disease and other neurodegenerative dementias in comorbidity: a clinical and neuropathological overview. *Clinical biochemistry* 73, 26–31.
- Miletić, S., Bazin, P.L., Isherwood, S.J., Keuken, M.C., Alkemade, A., Forstmann, B.U., 2022. Charting human subcortical maturation across the adult lifespan with in vivo 7 t mri. *NeuroImage* 249, 118872.
- Milletari, F., Navab, N., Ahmadi, S.A., 2016. V-net: Fully convolutional neural networks for volumetric medical image segmentation, in: 2016 fourth international conference on 3D vision (3DV), IEEE. pp. 565–571.
- Möller, C., Hafkemeijer, A., Pijnenburg, Y.A., Rombouts, S.A., van der Grond, J., Dopper, E., van Swieten, J., Versteeg, A., Pouwels, P.J., Barkhof, F., et al., 2015. Joint assessment of white matter integrity, cortical and subcortical atrophy to distinguish ad from behavioral variant ftd: A two-center study. *NeuroImage: Clinical* 9, 418–429.
- Negash, S., A Bennett, D., S Wilson, R., A Schneider, J., E Arnold, S., 2011. Cognition and neuropathology in aging: multidimensional perspectives from the rush religious orders study and rush memory and aging project. *Current Alzheimer Research* 8, 336–340.

- Ogniewicz, R.L., Ilg, M., 1992. Voronoi skeletons: theory and applications., in: CVPR, pp. 63–69.
- Ohm, D.T., Fought, A.J., Martersteck, A., Coventry, C., Sridhar, J., Gefen, T., Weintraub, S., Bigio, E., Mesulam, M.M., Rogalski, E., et al., 2021. Accumulation of neurofibrillary tangles and activated microglia is associated with lower neuron densities in the aphasic variant of alzheimer’s disease. *Brain Pathology* 31, 189–204.
- Oktay, O., Schlemper, J., Folgoc, L.L., Lee, M., Heinrich, M., Misawa, K., Mori, K., McDonagh, S., Hammerla, N.Y., Kainz, B., et al., 2018. Attention u-net: Learning where to look for the pancreas. *arXiv preprint arXiv:1804.03999* .
- Paaanen, T., Hänninen, T., Aitken, A., Hallikainen, M., Westman, E., Wahlund, L.O., Sobow, T., Mecocci, P., Tsolaki, M., Vellas, B., et al., 2013. Cerad neuropsychological total scores reflect cortical thinning in prodromal alzheimer’s disease. *Dementia and geriatric cognitive disorders extra* 3, 446–458.
- Pallebage-Gamarallage, M., Foxley, S., Menke, R.A., Huszar, I.N., Jenkinson, M., Tendler, B.C., Wang, C., Jbabdi, S., Turner, M.R., Miller, K.L., et al., 2018. Dissecting the pathobiology of altered mri signal in amyotrophic lateral sclerosis: A post mortem whole brain sampling strategy for the integration of ultra-high-field mri and quantitative neuropathology. *BMC neuroscience* 19, 1–24.
- Puonti, O., Iglesias, J.E., Van Leemput, K., 2016. Fast and sequence-adaptive whole-brain segmentation using parametric bayesian modeling. *NeuroImage* 143, 235–249.
- Ravikumar, S., Wisse, L.E., Ittyerah, R., Lim, S., Lavery, M., Xie, L., Robinson, J.L., Schuck, T., Grossman, M., Lee, E.B., et al., 2020. Building an ex vivo atlas of the earliest brain regions affected by alzheimer’s disease pathology, in: 2020 IEEE 17th International Symposium on Biomedical Imaging (ISBI), IEEE. pp. 113–117.

- Ravikumar, S., Wisse, L.E., Lim, S., Ittyerah, R., Xie, L., Bedard, M.L., Das, S.R., Lee, E.B., Tisdall, M.D., Prabhakaran, K., et al., 2021. Ex vivo mri atlas of the human medial temporal lobe: characterizing neurodegeneration due to tau pathology. *Acta neuropathologica communications* 9, 1–14.
- Reijmer, Y.D., Schultz, A.P., Leemans, A., O’sullivan, M., Gurol, M.E., Sperling, R., Greenberg, S.M., Viswanathan, A., Hedden, T., 2015. Decoupling of structural and functional brain connectivity in older adults with white matter hyperintensities. *Neuroimage* 117, 222–229.
- Rickmann, A.M., Roy, A.G., Sarasua, I., Navab, N., Wachinger, C., 2019. ‘project & excite’ modules for segmentation of volumetric medical scans, in: *International Conference on Medical Image Computing and Computer-Assisted Intervention*, Springer. pp. 39–47.
- Rizvi, B., Narkhede, A., Last, B.S., Budge, M., Tosto, G., Manly, J.J., Schupf, N., Mayeux, R., Brickman, A.M., 2018. The effect of white matter hyperintensities on cognition is mediated by cortical atrophy. *Neurobiology of aging* 64, 25–32.
- Robinson, J.L., Lee, E.B., Xie, S.X., Rennert, L., Suh, E., Bredenberg, C., Caswell, C., Van Deerlin, V.M., Yan, N., Yousef, A., et al., 2018. Neurodegenerative disease concomitant proteinopathies are prevalent, age-related and apoe4-associated. *Brain* 141, 2181–2193.
- Rohrer, J.D., Nicholas, J.M., Cash, D.M., van Swieten, J., Dopper, E., Jiskoot, L., van Minkelen, R., Rombouts, S.A., Cardoso, M.J., Clegg, S., et al., 2015. Presymptomatic cognitive and neuroanatomical changes in genetic frontotemporal dementia in the genetic frontotemporal dementia initiative (genfi) study: a cross-sectional analysis. *The Lancet Neurology* 14, 253–262.
- Roy, A.G., Navab, N., Wachinger, C., 2018. Recalibrating fully convolutional networks with spatial and channel “squeeze and excitation” blocks. *IEEE transactions on medical imaging* 38, 540–549.

- Sadaghiani, S., Trotman, W., Lim, S.A., Chung, E., Ittyerah, R., Ravikumar, S., Khandelwal, P., Prabhakaran, K., Lavery, M.L., Ohm, D.T., et al., 2022. Associations of phosphorylated tau pathology with whole-hemisphere ex vivo morphometry in 7 tesla mri. *Alzheimer's & Dementia* .
- Santos, V.D., Thomann, P.A., Wüstenberg, T., Seidl, U., Essig, M., Schröder, J., 2011. Morphological cerebral correlates of cerad test performance in mild cognitive impairment and alzheimer's disease. *Journal of Alzheimer's Disease* 23, 411–420.
- Schiffer, C., Amunts, K., Harmeling, S., Dickscheid, T., 2021a. Contrastive representation learning for whole brain cytoarchitectonic mapping in histological human brain sections, in: 2021 IEEE 18th International Symposium on Biomedical Imaging (ISBI), IEEE. pp. 603–606.
- Schiffer, C., Harmeling, S., Amunts, K., Dickscheid, T., 2021b. 2d histology meets 3d topology: Cytoarchitectonic brain mapping with graph neural networks, in: International Conference on Medical Image Computing and Computer-Assisted Intervention, Springer. pp. 395–404.
- Schiffer, C., Spitzer, H., Kiwitz, K., Unger, N., Wagstyl, K., Evans, A.C., Harmeling, S., Amunts, K., Dickscheid, T., 2021c. Convolutional neural networks for cytoarchitectonic brain mapping at large scale. *NeuroImage* 240, 118327.
- Schneider, J.A., Arvanitakis, Z., Bang, W., Bennett, D.A., 2007. Mixed brain pathologies account for most dementia cases in community-dwelling older persons. *Neurology* 69, 2197–2204.
- Spitzer, H., Kiwitz, K., Amunts, K., Harmeling, S., Dickscheid, T., 2018. Improving cytoarchitectonic segmentation of human brain areas with self-supervised siamese networks, in: International Conference on Medical Image Computing and Computer-Assisted Intervention, Springer. pp. 663–671.

- Tisdall, M.D., Ohm, D.T., Lobrovich, R., Das, S.R., et al., 2021. Joint ex vivo mri and histology detect iron-rich cortical gliosis in tau and tdp-43 proteinopathies. *bioRxiv* .
- Toledo, J.B., Van Deerlin, V.M., Lee, E.B., Suh, E., Baek, Y., Robinson, J.L., Xie, S.X., McBride, J., Wood, E.M., Schuck, T., et al., 2014. A platform for discovery: the university of pennsylvania integrated neurodegenerative disease biobank. *Alzheimer's & dementia* 10, 477–484.
- Ushizima, D., Chen, Y., Alegro, M., Ovando, D., Eser, R., Lee, W., Poon, K., Shankar, A., Kantamneni, N., Satrawada, S., et al., 2022. Deep learning for alzheimer's disease: Mapping large-scale histological tau protein for neuroimaging biomarker validation. *NeuroImage* 248, 118790.
- Vega, A.R., Chkheidze, R., Jarmale, V., Shang, P., Foong, C., Diamond, M.I., White, C.L., Rajaram, S., 2021. Deep learning reveals disease-specific signatures of white matter pathology in tauopathies. *Acta neuropathologica communications* 9, 1–13.
- Watanabe, R., Kawakami, I., Onaya, M., Higashi, S., Arai, N., Akiyama, H., Hasegawa, M., Arai, T., 2018. Frontotemporal dementia with trans-activation response dna-binding protein 43 presenting with catatonic syndrome. *Neuropathology* 38, 281–287.
- Whitwell, J.L., Graff-Radford, J., Tosakulwong, N., Weigand, S.D., Machulda, M.M., Senjem, M.L., Spychalla, A.J., Vemuri, P., Jones, D.T., Drubach, D.A., et al., 2018. Imaging correlations of tau, amyloid, metabolism, and atrophy in typical and atypical alzheimer's disease. *Alzheimer's & Dementia* 14, 1005–1014.
- Wisse, L., Adler, D., Ittyerah, R., Pluta, J., Robinson, J., Schuck, T., Trojanowski, J., Grossman, M., Detre, J., Elliott, M., et al., 2017. Comparison of in vivo and ex vivo mri of the human hippocampal formation in the same subjects. *Cerebral Cortex* 27, 5185–5196.

- Wisse, L., Ravikumar, S., Ittyerah, R., Lim, S., Lane, J., Bedard, M., Xie, L., Das, S., Schuck, T., Grossman, M., et al., 2021. Downstream effects of polypathology on neurodegeneration of medial temporal lobe subregions. *Acta neuropathologica communications* 9, 1–11.
- Wisse, L., Ravikumar, S., Ittyerah, R., Lim, S.A., Lane, J., Lavery, M., Xie, L., Robinson, J.L., Schuck, T., Grossman, M., et al., 2020. High-resolution postmortem mri reveals tdp-43 association with medial temporal lobe subregional atrophy: Biomarkers: Leveraging postmortem collections to validate neuroimaging. *Alzheimer's & Dementia* 16, e045744.
- Xia, C., Makaretz, S.J., Caso, C., McGinnis, S., Gomperts, S.N., Sepulcre, J., Gomez-Isla, T., Hyman, B.T., Schultz, A., Vasdev, N., et al., 2017. Association of in vivo [18f] av-1451 tau pet imaging results with cortical atrophy and symptoms in typical and atypical alzheimer disease. *JAMA neurology* 74, 427–436.
- Xie, L., Das, S.R., Wisse, L.E., Ittyerah, R., Yushkevich, P.A., Wolk, D.A., Initiative, A.D.N., et al., 2018. Early tau burden correlates with higher rate of atrophy in transentorhinal cortex. *Journal of Alzheimer's Disease* 62, 85–92.
- Xie, L., Wisse, L.E., Pluta, J., de Flores, R., Piskin, V., Manjón, J.V., Wang, H., Das, S.R., Ding, S.L., Wolk, D.A., et al., 2019. Automated segmentation of medial temporal lobe subregions on in vivo t1-weighted mri in early stages of alzheimer's disease. *Human brain mapping* 40, 3431–3451.
- Yushkevich, P.A., López, M.M., Martin, M.M.I.d.O., Ittyerah, R., Lim, S., Ravikumar, S., Bedard, M.L., Pickup, S., Liu, W., Wang, J., et al., 2021. Three-dimensional mapping of neurofibrillary tangle burden in the human medial temporal lobe. *Brain* .
- Yushkevich, P.A., Pashchinskiy, A., Oguz, I., Mohan, S., Schmitt, J.E., Stein, J.M., Zukić, D., Vicory, J., McCormick, M., Yushkevich, N., et al., 2019. User-guided segmentation of multi-modality medical imaging datasets with itk-snap. *Neuroinformatics* 17, 83–102.

Yushkevich, P.A., Pluta, J.B., Wang, H., Xie, L., Ding, S.L., Gertje, E.C., Mancuso, L., Klot, D., Das, S.R., Wolk, D.A., 2015. Automated volumetry and regional thickness analysis of hippocampal subfields and medial temporal cortical structures in mild cognitive impairment. *Human brain mapping* 36, 258–287.

Zhu, W., Huang, Y., Zeng, L., Chen, X., Liu, Y., Qian, Z., Du, N., Fan, W., Xie, X., 2019. Anatomynet: deep learning for fast and fully automated whole-volume segmentation of head and neck anatomy. *Medical physics* 46, 576–589.

## SUPPLEMENTAL MATERIAL

### Architectural details of the nine neural networks

**3D Unet-like:** We implement a custom in-house 3D Unet-like architecture Khandelwal and Yushkevich (2020), where the input and the output have dimensions  $in \times H \times W \times D$ , and  $out \times H \times W \times D$ . The first dimension represents the number of channels, and H, W and D denote the height, width and depth respectively. There are five encoder blocks (with the last block acting as the bottleneck layer), and four decoder blocks, with skip connections. We have used *groupnorm* as the normalization method. Note that the first encoder block does not consist the MaxPool operation, and the first decoder block does not consist the first set of conv3D, groupnorm, and ReLU units. The **encoder** block has the following *output* dimensions at each of the encoder block: E1:  $16 \times H \times W \times D$ , E2:  $32 \times \frac{H}{2} \times \frac{W}{2} \times \frac{D}{2}$ , E3:  $64 \times \frac{H}{4} \times \frac{W}{4} \times \frac{D}{4}$ , E4:  $128 \times \frac{H}{8} \times \frac{W}{8} \times \frac{D}{8}$ , E5:  $256 \times \frac{H}{16} \times \frac{W}{16} \times \frac{D}{16}$ . The **decoder** block has the following *output* dimensions at each of the decoder block: D1:  $256 \times \frac{H}{8} \times \frac{W}{8} \times \frac{D}{8}$ , D2:  $128 \times \frac{H}{4} \times \frac{W}{4} \times \frac{D}{4}$ , D3:  $64 \times \frac{H}{2} \times \frac{W}{2} \times \frac{D}{2}$ , D4:  $32 \times H \times W \times D$ .

**VNet:** We implement the following variant of VNet Milletari et al. (2016). The input and the output volumes have dimensions  $in \times H \times W \times D$  (here:  $in$  is 1), and  $out \times H \times W \times D$  respectively, where  $out$  represents the number of output classes. We have four different modules: an InputTransition, DownTransition, UpTransition, and OutputTransition. The InputTransition comprises of a 3D convolution block with input channels  $in$  and produces  $ch$  output channels by using a kernel size of 5 and padding of 2, followed by BatchNorm. Next, the input is added to the output of the convolutional block to obtain a residual function and then followed by PReLU, to produce an output with dimensions,  $ch \times H \times W \times D$ . This output is then fed to the first DownTransition module. The DownTransition block consists of 3D convolution block, with kernel size of 2 and stride of 2, which takes in the input  $ch \times H \times W \times D$  and downsamples the feature map by a factor of 2 and doubles the number of channels, thus giving an output of  $(2 \times ch) \times \frac{H}{2} \times \frac{W}{2} \times \frac{D}{2}$ , which is then followed by BatchNorm and PReLU

nonlinearity and an optional dropout. A residual function is then created by using another convolutional block by using a kernel size of 5 and padding of 2, followed by PReLU nonlinearity. The second DownTransition block produces an output of  $(4 \times ch) \times \frac{H}{4} \times \frac{W}{4} \times \frac{D}{4}$ . The third and fourth DownTransition blocks has the dropout set to True and produces an output of  $(8 \times ch) \times \frac{H}{8} \times \frac{W}{8} \times \frac{D}{8}$  and  $(16 \times ch) \times \frac{H}{16} \times \frac{W}{16} \times \frac{D}{16}$  respectively. The UpTransition block is similar to the DownTransition with the difference that every block upsamples the input using 3D transpose convolutions, and has skip connections like UNet from the corresponding DownTransition block. The first UpTransition block upsamples from  $(16 \times ch) \times \frac{H}{16} \times \frac{W}{16} \times \frac{D}{16}$  to  $(16 \times ch) \times \frac{H}{8} \times \frac{W}{8} \times \frac{D}{8}$  with dropout set to true. The next UpTransition block upsamples to  $(8 \times ch) \times \frac{H}{4} \times \frac{W}{4} \times \frac{D}{4}$  with dropout set to true. The next two UpTransition blocks produces an output of  $(4 \times ch) \times \frac{H}{2} \times \frac{W}{2} \times \frac{D}{2}$  and  $(2 \times ch) \times H \times W \times D$  respectively. Finally, the last block OutputTransition produces the desired output of  $out \times H \times W \times D$  using two 3D convolutional layers.

**VoxResNet:** We implement the following variant of VoxResNet Chen et al. (2018). In our implementation, we define a building block called VoxRes, which creates a residual function, comprising two sets of BatchNorm, ReLU and 3D convolution with kernel size of 3, stride of 1 and padding of 1. In the VoxResNet architecture, there are four encoder and four decoder blocks. The first encoder block consists of a 3D convolution with kernel size 3 and padding of 1, BatchNorm, ReLU and 3D convolution, thus changing the input of  $in \times H \times W \times D$  to  $ch \times H \times W \times D$ , where  $ch=32$ . The next three encoder block successively down-samples the input from  $ch \times H \times W \times D$  to  $(2 \times ch) \times \frac{H}{2} \times \frac{W}{2} \times \frac{D}{2}$ ,  $(2 \times ch) \times \frac{H}{4} \times \frac{W}{4} \times \frac{D}{4}$  and  $(2 \times ch) \times \frac{H}{8} \times \frac{W}{8} \times \frac{D}{8}$  respectively by stacking BatchNorm, ReLU, 3D convolution, with kernel size of 3, stride of (1, 2, 2) and padding of 1, and VoxResNet module. The four decoder blocks takes in the output of the corresponding encoder block. The decoder block transforms the output of the first encoder from  $ch \times H \times W \times D$  to  $ch \times H \times W \times D$  using transposed convolution and then from  $ch \times H \times W \times D$  to  $out \times H \times W \times D$  using convolution where  $out$  represents the number of output classes. The second decoder block takes in output from the corresponding encoder block to produce an output from  $(2 \times ch) \times \frac{H}{2} \times \frac{W}{2} \times \frac{D}{2}$  to

$outxHxWxD$  using transposed convolution with 64 filters and a 3D convolution with kernel of (1, 2, 2) and stride of (1, 2, 2). Similarly, the third and fourth decoder block takes in output from the corresponding encoder block to produce an output from  $(2 \times ch) \times \frac{H}{4} \times \frac{W}{4} \times \frac{D}{4}$  to  $outxHxWxD$  using transposed convolution with 64 filters with kernel of (1, 4, 4) and stride of (1, 4, 4) and a 3D convolution; and from  $(2 \times ch) \times \frac{H}{8} \times \frac{W}{8} \times \frac{D}{8}$  to  $outxHxWxD$  using transposed convolution with 64 filters with kernel of (1, 8, 8) and stride of (1, 8, 8) and a 3D convolution. The outputs from the four decoder blocks are then added element-wise to produce the final output of size  $outxHxWxD$ .

**Attention U-Net:** The building block of Attention U-Net Oktay et al. (2018) is the AttentionGate module which comprises of a gating mechanism to suppress irrelevant background. The AttentionGate takes in two volumes  $G$  and  $X$ , of size  $ch_g \times H_g \times W_g \times D_g$  and  $ch_x \times H_x \times W_x \times D_x$  respectively, and produce outputs of size  $ch_{inter} \times H_g \times W_g \times D_g$  using 3D convolutions with kernel size and padding of 1. The two outputs are then summed up element-wise and passed through ReLU activation, followed by another convolution, with kernel size and padding of 1, and a sigmoid activation function. Finally, this output is upsampled and then multiplied by the input volume  $X$  to  $ch_x \times H_x \times W_x \times D_x$  to produce the final volume,  $\hat{X}$ , with dimensions  $ch_x \times H_x \times W_x \times D_x$ .

The Attention U-Net architecture mimics a standard U-Net with an AttentionGate mechanism taking in input from the decoder's output for up-sampling and the corresponding encoder. The four encoder blocks take in the volume of  $inxHxWxD$ , where  $in$  is 1, and successively reduce the resolution to  $(64 \times ch) \times \frac{H}{2} \times \frac{W}{2} \times \frac{D}{2}$ ,  $(128 \times ch) \times \frac{H}{4} \times \frac{W}{4} \times \frac{D}{4}$ ,  $(256 \times ch) \times \frac{H}{8} \times \frac{W}{8} \times \frac{D}{8}$ , and  $(512 \times ch) \times \frac{H}{16} \times \frac{W}{16} \times \frac{D}{16}$  by using convolution block comprising of a stack of two convolutions with kernel size of (2,2,2) and two ReLU layers.

Now, the first AttentionGate takes in as inputs, the outputs of the third and the fourth encoder blocks, and produces an output of dimension  $(256 \times ch) \times \frac{H}{8} \times \frac{W}{8} \times \frac{D}{8}$ , which is then concatenated with the upsampled version of the output of the fourth encoder block  $(256 \times ch) \times \frac{H}{8} \times \frac{W}{8} \times \frac{D}{8}$ , and then this output is again upsampled to  $(128 \times ch) \times \frac{H}{8} \times \frac{W}{8} \times \frac{D}{8}$ . This procedure is repeated two more

times to get output dimensions of  $(64 \times ch) \times \frac{H}{4} \times \frac{W}{4} \times \frac{D}{4}$  and  $(64 \times ch) \times \frac{H}{2} \times \frac{W}{2} \times \frac{D}{2}$  respectively. A final upsampling block then produces the desired output of  $out \times H \times W \times D$ .

**AnatomyNet (Vanilla):** AnatomyNet Zhu et al. (2019) is a variant of U-Net which takes advantage of the Squeeze-and-Excitation residual feature (SE) blocks proposed in Rickmann et al. (2019); Roy et al. (2018) to segment small anatomical structures, which are often missed by networks such as U-Net. We implement four variants of the AnatomyNet, with the first variant AnatomyNet (Vanilla) without any SE blocks. The first block takes an input with size  $in \times H \times W \times D$  and generates a feature map of size  $ch \times H \times W \times D$ , here  $in$  is 1 and  $ch$  is 28, using 3D convolution with kernel size of 3, stride of 2, and padding of 1; followed by a BatchNorm and LeakyReLU activation layer.

The next three blocks take in the input  $ch \times H \times W \times D$ , and successively increase the feature channels and downsamples by 2 from  $(28) \times H \times W \times D$  to  $(34) \times \frac{H}{2} \times \frac{W}{2} \times \frac{D}{2}$ . Each of these three blocks consists of two repetitions of a ResidualBasicBlock. The ResidualBasicBlock comprises of a 3D convolution with kernel size of 3, stride of 2, and padding of 1, followed by BatchNorm, LeakyReLU, 3D convolution with kernel size of 3, stride of 2, and padding of 1, BatchNorm, SEBlock and a downsampling 3D convolution with kernel size of 3, stride of 1. The SEBlock consists of one of the three variants of the Squeeze-and-Excitation blocks: Spatial Excitation AnatomyNet (SE), Channel Excitation AnatomyNet (CE) or the Channel-spatial Excitation AnatomyNet (CE + SE). But, here we do not include the SEBlock in the ResidualBasicBlock in the AnatomyNet (Vanilla) variant.

The next block in the network architecture is the ResidualUPBasicBlock, which concatenates two inputs of size  $(34) \times \frac{H}{2} \times \frac{W}{2} \times \frac{D}{2}$  and  $(32) \times \frac{H}{2} \times \frac{W}{2} \times \frac{D}{2}$  to produce  $(66) \times \frac{H}{2} \times \frac{W}{2} \times \frac{D}{2}$ , followed by a 3D convolution with kernel size of 3, stride of 2, and padding of 1, followed by BatchNorm, LeakyReLU, 3D convolution with kernel size of 3, stride of 2, and padding of 1, BatchNorm, SEBlock and a down-sampling 3D convolution with kernel size of 3 and stride of 1, and LeakyReLU to produce  $(32) \times \frac{H}{2} \times \frac{W}{2} \times \frac{D}{2}$ . This is followed by three sets of ResidualBasicBlock,

without the downsampling layer, and the ResidualUPBasicBlock to produce an output of size  $(14) \times H \times W \times D$ . A final 3D convolution is employed to produce the output of  $(out) \times H \times W \times D$ , where *out* is the number of segmentation classes.

**Channel Squeeze and Spatial Excitation AnatomyNet (sSE):** The architecture of the Channel Squeeze and Spatial Excitation AnatomyNet (sSE) is similar to the *Vanilla* variant, with the only difference being that the SEBlock consists of Spatial excitation module. The SEBlock squeezes the feature maps along the channel dimension and excites the spatial dimension. This block helps in segmentation of fine-grained structures as proposed in Roy et al. (2018). This block consists of a 3D convolution with kernel size of 1 and stride of 1, followed by a Sigmoid activation layer which takes an input with  $ch$  channels,  $ch \times H \times W \times D$ , and reduces it to  $1 \times H \times W \times D$ . The channel-squeezed output is then multiplied element-wise with the input feature map to produce the spatial-excited feature map of dimension  $ch \times H \times W \times D$ .

**Spatial Squeeze and Channel Excitation AnatomyNet (cSE):** The architecture of the Spatial Squeeze and Channel Excitation AnatomyNet (cSE) is similar to the *Vanilla* variant, with the only difference being that the SEBlock consists of a Channel excitation module. This SEBlock consists of the following layers: the spatial channels of dimension  $ch \times H \times W \times D$ , which is spatially squeezed to  $ch \times 1 \times 1 \times 1$  using adaptive pooling. Two layers of fully connected layer and ReLU activation function transforms this feature map to a vector of length  $ch$ . This feature map is then element-wise multiplied with the original input feature map to produce a channel-excited map of  $ch \times H \times W \times D$ .

**Spatial and Channel Squeeze and Excitation AnatomyNet (scSE):** The architecture of the Spatial excitation AnatomyNet (SE) is similar to the *Vanilla* variant, with the only difference being that the SEBlock consists of Channel-spatial excitation module. The input tensor of size  $ch \times H \times W \times D$  is passed through both *cSE* and *sSE*. An element-wise max is taken between these feature maps to produce the final output of size  $ch \times H \times W \times D$ .

**nnU-Net:** We use the default network in the nnU-Net framework as described in Isensee et al Isensee et al. (2021).

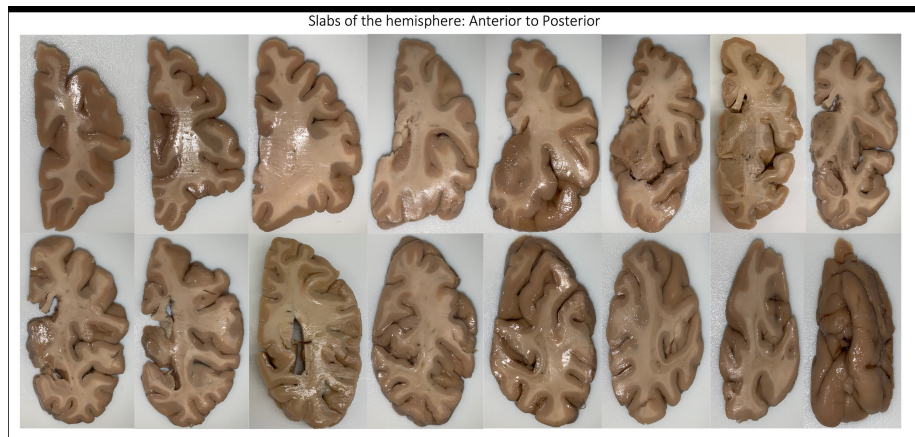


Figure 1: Post-mortem tissue blockface photograph of a white female with Parkinson's disease (not demented) and Lewy body disease, deceased at the age of 79. Shown are the slabbed blockface images from anterior to posterior.

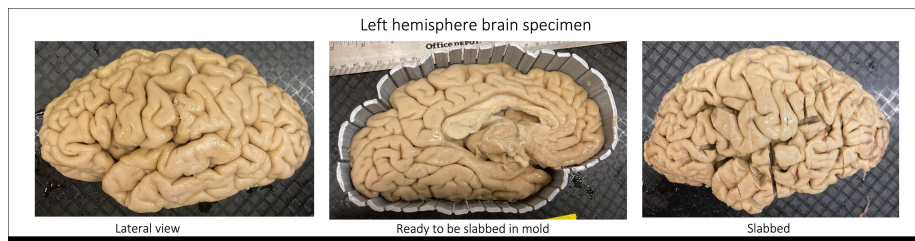


Figure 2: Post-mortem tissue blockface photograph of a patient with FTLN primary-progressive-aphasia (PNFA) and Globular glial tauopathy (GGT) disease, deceased at the age of 74. Shown are the lateral and medial views of the left hemisphere. The tissue is then placed in a mold and is subsequently slabbed.

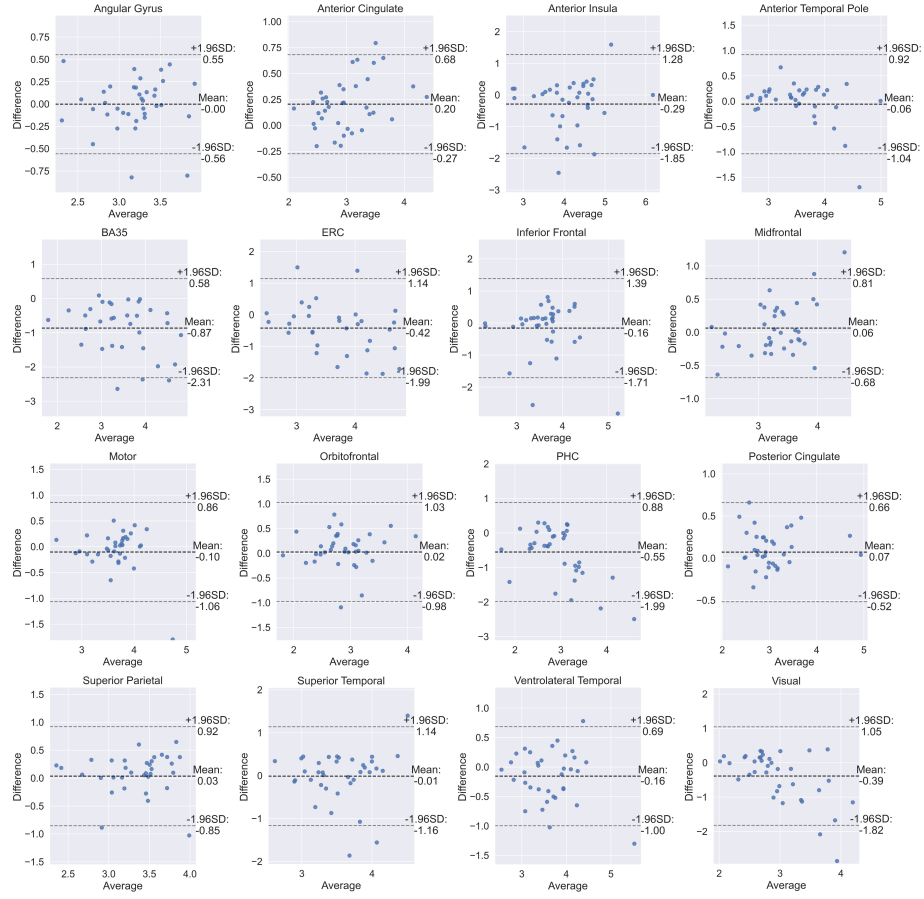


Figure 3: Bland-Altman plots for the cortical regions. We observe good agreement between the manual and automated segmentations-based thickness, which supports the hypothesis that deep learning-based automated segmentations are reliable for morphometric measurements.

Table 1: Demographics of the Alzheimer’s Disease and Related Dementia (ADRD) patient cohort used in the current study. The mean age of females (N=12) was  $75.42 \pm 8.62$  years compared to  $76.68 \pm 11.67$  years that of males (N=25), with an overall age of  $74.55 \pm 10.94$  years. Abbreviations: AD: Alzheimer’s Disease, ALS: Amyotrophic lateral sclerosis, CVD: Cerebrovascular Disease, LATE: Limbic-predominant Age-related TDP-tau 43 Encephalopathy, LBD: Lewy Body Disease, CTE:, FTLD-TDP: Frontotemporal lobar degeneration with TDP inclusions, GGT: Globular glial p-tauopathy, CVD: Cerebrovascular Disease, CBD: Corticobasal degeneration, PART: Primary age-related p-tauopathy, PSP: Progressive supranuclear palsy, p-tau-Misc: p-tauopathy unclassifiable. Note that subject 38 in the table below was not used for any correlation analyses in the current study.

Subject	AD Spectrum	Primary	Secondary	Age	Race	Sex	Cortex cross-val	Subcortical cross-val	WMH cross-val	WM
1	Yes	AD	CVD+AD	87	White	M				
2	Yes	AD	LATE+AD	87	White	M			Y	
3	Yes	AD	AD	98	White	M				
4	Yes	AD	LATE+AD	89	White	F		Y		Y
5	Yes	AD	AD	88	White	M				
6	Yes	AD	CVD+AD	75	Black	F				
7	Yes	AD	LATE+AD	84	White	M				
8	Yes	AD	LATE+AD	75	White	F				
9	Yes	AD	LBD+LATE+AD	63	White	F			Y	
10	Yes	AD	AD+LATE	74	White	F				
11	Yes	AD	AD	99	White	M				
12	Yes	AD	AD	75	White	M				
13	Yes	AD	AD	73	White	M	Y	Y	Y	
14	Yes	LBD	LBD+AD	97	White	M				
15	Yes	LBD	LBD+AD	95	White	F				
16	Yes	LBD	LBD+AD+CVD+CTE	74	White	M				
17	Yes	LBD	LBD+AD+CTE	71	White	M	Y	Y	Y	
18	Yes	LBD	LBD+AD	69	White	M				
19	Yes	LBD	LBD+AD	76	White	M				
20	Yes	LBD	LBD+AD	73	Black	M	Y	Y	Y	
21	Yes	LBD	LBD+AD	66	NA	F				
22	No	FTLD-TDP	FTLD-TDP43	74	White	F				
23	No	FTLD-TDP	FTLD-TDP43	70	White	M				
24	No	FTLD-TDP	FTLD-TDP43+AD	72	White	M				
25	No	FTLD-TDP	FTLD-TDP43+ALS+LBD+AD	54	White	M				
26	No	FTLD-TDP	FTLD-TDP43	65	White	M	Y	Y	Y	
27	No	FTLD-TDP	FTLD-TDP43+LATE+AD	69	White	M				
28	No	FTLD-TDP	FTLD-TDP43+LATE+CVD+AD	78	White	M				
29	No	FTLD-TDP	FTLD+AD	81	White	M	Y	Y		
30	No	Tau-Misc	Tau+AD	67	White	F				
31	No	Tau-Misc	FTLD	50	White	M			Y	
32	Yes	Tau-Misc	PART+CVD	76	Black	F				
33	No	Tau-4R	GGT	74	White	F				
34	No	Tau-4R	GGT	77	White	M				
35	No	Tau-4R	CBD	77	White	F	Y	Y		Y
36	No	Tau-4R	PSP+AD	74	White	M				
37	No	Tau-4R	CBD+AD	76	White	M			Y	
38	Yes	AD	LATE+AD	83	White	F			Y	

Table 2: The locations from where the neuropathology ratings were obtained from, either the exact (main regions) or the closest (exploratory regions), to the cortical brain regions.

Brain region	Matching pathology region	Exact
Visual cortex	Occipital cortex	Y
Middle frontal gyrus	Middle frontal gyrus	Y
Orbitofrontal gyrus	Orbital frontal cortex	Y
Anterior cingulate	Cingulate gyrus	Y
Posterior cingulate	Cingulate gyrus	Y
Motor cortex	Motor cortex	Y
Angular gyrus	Angular gyrus	Y
Superior parietal cortex	Angular gyrus	N
Superior temporal cortex	Superior/ middle temporal	Y
Anterior temporal pole	Amygdala	N
Anterior insula	Middle frontal gyrus	N
Ventrolateral part of anterior temporal cortex (Inferior temporal gyrus)	Entorhinal cortex	N
Inferior frontal cortex (Broca's area)	Middle frontal gyrus	N
Entorhinal cortex	Entorhinal cortex	Y
Brodmann area 35	Entorhinal cortex	Y
Parahippocampal cortex	CA1/ Subiculum	N